ORIGINAL PAPER

Mustafa Eroğlu [ID] · İsmail Esen · Mehmet Akif Koç

Thermal vibration and buckling analysis of magneto-electro-elastic functionally graded porous higher-order nanobeams using nonlocal strain gradient theory

Abstract In this paper, free vibration analysis and temperature-dependent buckling behavior of porous functionally graded magneto-electro-thermo-elastic material consisting of cobalt ferrite and barium titanate were modeled and analyzed. A high-order sinusoidal shear deformation theory was used to accurately model the anisotropic material behavior. The study examined the porosity role variation across thickness in the buckling and free vibration behavior of nanobeams, as well as the effects of magneto-electro-elastic coupling, thermal stresses, nonlocal properties, externally applied electric and magnetic field potential, and porosity volume fraction.

1 Introduction

Functionally graded composite materials have been a significant research topic in numerous engineering fields over the last decade. The mechanical properties required in various research fields are difficult to combine. Therefore, it is crucial to use intelligent materials, such as magneto-electro-thermo-elastic materials (METE). Such materials can transform into more valuable materials by using magnetic, electrical, thermal, and mechanical energies and are known as functionally graded materials (FGMs) to meet properties such as thermal resistance and high strength in the industry. The mechanical characteristics of FGMs, which typically consist of two distinct parts, change seamlessly between one another, leading to the creation of new structures that can withstand a range of loads [1]. These two materials are mainly barium titanate ($BaTiO_3$), which is a ferroelectric ceramic material with piezoelectric and photorefractive properties, and cobalt ferrite ($CoFe_2O_4$), which has magnetostrictive properties [2]. As a result, while the latter may be preferred for electromechanical converters and capacitors, the former may be selected for actuators and sensors.

Because it is difficult to predict the small structures's mechanical behavior using classical mechanics theories, there are theories in the literature to analyze micro- or nanosized structures. Some of these are theories such as nonlocal elasticity [3], strain gradient [4–6], and nonlocal strain gradient elasticity [7–12]. Nonlocal elasticity theory (NET), which is widely used today, was proposed by Eringen in 1983 [13]. According to this theory, as the size of the material decreases, it expresses its softness according to a nonlocal parameter, and it is a value ranging from 0 to 4 nm^2. Using Eringen's nonlocal elasticity theory, Ebrahimi and Barati investigated the thermal buckling of nonlocal magneto-electro-thermo-elastic FG beams [14]. Magnetic-electric-thermo-elastic functionally graded plates (METE-FGPPs) exposed to supersonic airflow were the subject of a study by

M. Eroğlu (✉)
Engineering Faculty, Mechanical Engineering Department, Sakarya University, 54187 Sakarya, Turkey
e-mail: mustafaeroglu@sakarya.edu.tr

İsmail Esen
Engineering Faculty, Mechanical Engineering Department, Karabük University, 78050 Karabük, Turkey

M. A. Koç
Technology Faculty, Mechatronics Engineering Department, Sakarya Applied Sciences University, 54187 Sakarya, Turkey

Zhong et al. on flutter instability [15]. Based on the trigonometric shear strain beam and modified double stress theories, Akgöz and Civalek et al. [16] realized a dimensional buckling analysis of embedded FG microbeams in a thermal environment. In a different study, they conducted the thick microbeam model using modified strain gradient and hyperbolic shear deformation beam theories, as well as the buckling behavior of two-parameter carbon nanotubes dependent on the microstructure [17, 18]. Eringen's nonlocal elasticity theory is employed to study the buckling, bending, and free vibration of Timoshenko nanobeams [19–21]. The same approach can be used to perform free, static, and thermal vibration analyses of nanoplates [22–28]. Li et al. examined the impact of scale on the free vibration analysis of FG nano-/microscale beams [29]. In a thermal environment, Chen et al. looked into the vibrations of functional stepped (FG) rotary pre-twisted sandwich blades [30]. Some FGM beam and plate studies [31–41] applying the small-size, magnetic field, viscoelastic foundation effects are interesting. Additionally, for large-sized beam and plate structures the following studies [42–54] have investigated the effects of porosity, FGM, and sigmoid distributions using analytical and FEM methods.

Cheshmeh et al. investigated the vibration and buckling responses of rectangular FG-CNTRC plates when subjected to thermomechanical load [55]. Esen and Özmen developed a model to simulate the thermal buckling and vibration behavior of a porous nanoplate made of functional grades of $CoFe_2O_4$ and $BaTiO_3$ [56]. Vaezi et al. calculated the critical magnetic and electric potential values by examining the free vibrations of MEE microbeams [57]. Toro et al. looked at coupled magneto-electro-elastic waves propagating along a periodic layered waveguide [58]. The nonlinear magneto-electro-elastic vibration of the smart sandwich plate is addressed analytically by Dat et al. [59]. Ke et al. [60] investigated how temperature changes affected microbeam free vibration and buckling. In their study, Eltaher et al. employ the finite element method to conduct a comprehensive analysis on the free vibration characteristics of functionally graded (FG) nanobeams with size-dependent behavior [61]. In a hygrothermal environment, Monaco et al. investigated nanoplates' buckling and linear vibrations [62]. A double girder system supported on an elastic foundation is studied by Chen et al. in terms of its buckling and post-buckling behavior [63]. Also, Daghigh et al. [64] analyzed the bending and buckling of carbon nanotube. Boyina et al. [65] devised a nonlocal strain gradient model for functionally graded Euler–Bernoulli beam buckling analysis under thermomechanical stresses. Quan et al. [66] provided analytical solutions for the examination of static buckling and vibration in nanocomposite multilayer perovskite solar cells.

It is a possible problem that porosity occurs due to the inevitable thermochemical reaction of materials with the environment and other additives in production. As a result, the dynamic and static behavior of FG composite should take distribution function and porosity within the structure into account. In this context, Kiran and Kattimani preferred the finite element method to research the free vibration properties and static behavior of a porous functional-grade magneto-electro-elastic plate [67]. Liu et al. solved the magneto-electro-elastic plate deformations with nonuniform materials [68]. Ebrahimi et al. investigated the free vibration of magneto-electroporous FG plates supported by elastic foundations with varying boundary conditions [69]. In the framework of isogeometric analysis, Xue et al. looked into the free vibration of the porous square, circular, and rectangular plates with a circular hole in the center [70]. Wang and Zu [71] established their structure based on the vibrations of rectangular plates of functionally graded material (FGM) acting in a porous and thermal environment. Li et al. [72] presented a successful method for the vibration of FGBs resting on Pasternak elastic foundations with continuously and arbitrarily varying cross sections. Kumar and Harsha used finite element formulations to investigate the vibration response of electro-thermally charged porous functionally graded piezoelectric plates [73]. Gholi et al. [74] studied the frequency response of a functionally graded (FG) porous annular plate covered with two piezo-electromagnetic layers. Sui et al. investigated the frictional contact that occurs in three dimensions (3D) when an electromagnetic field is applied to a magneto-electro-elastic (MEE) material and a rigid spherical punch [75]. Esmaeilzadeh and Kadkhodayan investigated the nonlinear transient response of a mobile porous microsized sandwich plate [76]. Based on first-order shear deformation theory, Bui et al. performed stochastic vibration and buckling analysis on I-section, functionally graded sandwich thin-walled beams [77]. Xu et al. [78] investigated the influence of the distribution of nanovoids related to trigonometric functions on the forced mechanical characteristics of functionally graded curved nanobeams. Ebrahimi and Hosseini [79] studied the performance of nano-electro-mechanical systems concerning primary and secondary resonances. Li et al. [80] conducted the acoustic radiation and vibration behavior of functionally graded magneto-electro-thermoelastic porous plates (METE-FGPPs). The thermal vibrational characteristics of a functionally graded porous graded cylindrical shell (FGP-SCS) were presented by Li et al. [81]. Using functionally graded (FG) porous beams with an uneven pore distribution, Chen et al. [82] investigated the forced and free vibration properties. According to nonlocal strain gradient theory, Majdi et al. [83] examined the forced and free vibrations of bidirectional functionally graded (BDFG) porous nanobeams under live loads

Table 1 Temperature-dependent coefficients for the properties of CoFe2O4 and BaTiO3

Material	Property	P_{-1}	P_0	P_1	P_2	P_3
CoFe$_2$O$_4$	C_{11}(Pa)	0	298.87e9	$-1.552e-4$	$6.125e-9$	$-9.0e-11$
	C_{55}(Pa)	0	47.33e9	$-1.552e-4$	$6.125e-9$	$-9.0e-11$
	υ	0	0.3	0	0	0
	$\alpha\left(1\text{K}^{-1}\right)$	0	$7.5e-6$	$-3.01e-4$	$4.02e-6$	$-1.01e-09$
	κ(W/mK)	0	4.7030	-0.0011	$1.6612e-06$	$-9.9670e-10$
	ρ (kg/m^3)	0	5300	0	0	0
BaTiO$_3$	C_{11}(Pa)	0	174e9	$-1.552e-4$	$6.125e-9$	$-9.0e-11$
	C_{55}(Pa)	0	44.93e9	$-1.552e-4$	$6.125e-9$	$-9.0e-11$
	υ	0	0.30	0	0	0
	$\alpha\left(1\text{K}^{-1}\right)$	0	$10e-6$	$-3.0e-4$	$4.0e-6$	$-1.0e-09$
	κ(W/mK)	0	3.7624	$-8.50521e-4$	$1.32894e-06$	$-7.97363e-10$
	ρ (kg/m^3)	0	5800	0	0	0

while taking the thickness effect into account. Karami et al. [84] studied the free vibration of nonuniform nanosized beams in a thermal environment using nonlocal strain gradient theory. Lu et al. [85] investigated a size-dependent sinusoidal shear strain beam model for free vibration of nanobeams. According to the two-phase local/nonlocal strain and stress gradient theory, Yang et al. [86] developed a unified high-order nanobeam model that takes into account a variety of high-order shear deformation beam theories in order to investigate the vibration response of the nanobeam. Vinh and Tounsi [87] used nonlocal first-order shear deformation theory to study functionally graded bi-curved nanoshells' free vibration. Civalek et al. [88] examined how deformable border and porosity affect the free vibration parameters of metal foam functionally graded restricted Rayleigh microbeams. Khoa examined FG laminated composite panel free vibration and nonlinear dynamics in hygrothermal conditions [89]. Mellal et al. [90] used high-order shear deformation theory (HSDT) to analyze the free vibration and stability of perfect and imperfect functionally graded (FG) beams. Karami and Janghorban presented the Timoshenko beam model with nonlocal strain gradient that accounts for axially varying materials and thickness terms to analyze the free vibrations of such nanotubes [91].

The literature shows the free vibration behavior of beams composed of magneto-electro-elastic materials, as seen above. However, most of the literature studies are given by taking into consideration simple conditions. In experimental literature studies [56, 92], it has been reported that porosity can occur up to 40% in BaTiO$_3$ and CoFe$_2$O$_4$ structures. For this reason, in this study, first, porosity and three different distribution forms of porosity, which can be formed in the production of ceramic materials BaTiO$_3$ and CoFe$_2$O$_4$, were taken into account. Since the behavior of nanosensors changes depending on the temperature in high-temperature applications, the nonlinear temperature distribution inside the nanosensor is taken into account in this study. The temperature-dependent material properties of BaTiO$_3$ and CoFe$_2$O$_4$ have been considered in nanosensor dynamics. Temperature-dependent nonlinear material properties were obtained using past experimental studies and presented in Table 1. Using a higher-order shear deformation theory, the dynamic behavior of porous nanobeam made of functional-grade BaTiO$_3$ and CoFe$_2$O$_4$ components was modeled and investigated using nonlocal strain gradient elasticity theory (NSGT). The free vibration behavior of the nanosensor beam, which consists of functional grading of BaTiO$_3$ and CoFe$_2$O$_4$, depending on temperature, material composition, porosity amount and porosity distribution, applied voltage, and magnetic field potentials, has been investigated with extensive analyzes, and the results are presented. The results of this study will be helpful in terms of obtaining accurate results in the design and analysis of micro-electro-mechanical system (MEMS) and nano-electro-mechanical system (NEMS) systems such as nano-/microsensors and nano-/microactuators. In addition, the results of this study are at a level that can be used in other applications such as wearable technology, nanodrug delivery, and high-performance aerospace applications under severe temperature conditions. Moreover, the implementation of porous nanobeams holds significant potential in various crucial domains, including nano- and microsurgery, surrounding fluid sampling and analysis, and precise delivery of essential fluids to specific treatment regions. Furthermore, they can be utilized in cold and hot gas analysis sensors, as well as in the measurement and regulation of ambient atmosphere within blast furnaces.
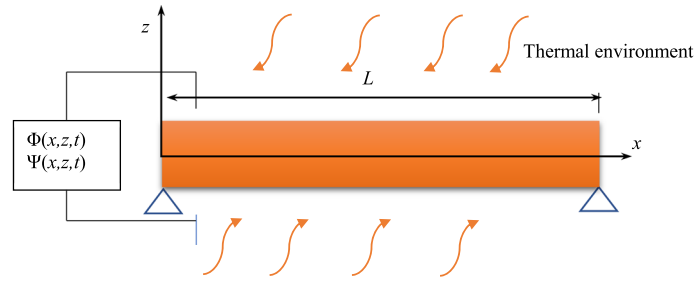
Fig. 1 A FG porous magneto-electro-elastic (MEE) nanosensor beam under electro-magnetic field

2 Theoretical formulation

2.1 The material properties of magneto-electro-viscoelastic FG nanobeam

Think about a beam of a magneto-electro-elastic functionally graded nanosensor and a fixed substrate with the specifications shown in Fig. 1. The $BaTiO_3$ and $CoFe_2O_4$ materials in the nanobeam, which have the temperature-dependent properties listed in Table 1, are exposed to a magnetic potential of γ (x, z, t) and an electric potential of $\Phi(x, z, t)$. Another electric potential $\Phi_a(x, z, t)$ between the beam and substrate is used to activate the nanosensor beam. According to a power-law distribution, the thickness direction of the effective material properties of nanobeams continuously changes as [93]

$$P(z) = [P_t - P_b]V_t + P_b$$
$$V_t = \left(\frac{z}{h} + \frac{1}{2}\right)^P, V_t + V_b = 1 \tag{1}$$

Here, the material grading index ($p \geq 0$), which controls how much material is distributed throughout the thickness, is present. The top and bottom sides' respective material properties are P_t and P_b. Please be aware that the bottom surface of the nanobeam ($z = h/2$) is fully $BaTiO_3$, while the top surface at $z = + h/2$ is fully $CoFe_2O_4$.

Because of the sintering process, the porosity of ceramic beams is sometimes unavoidable. As a result, porosity is considered in this study, and the distribution of porosity along thickness is presumable to be one of the types shown in Fig. 2. In particular, the relation shown below can be used to define the effective material proportions when the uniform porosity in Fig. 2a is taken into account: [93]

$$P(z) = [P_t - P_b]V_t + P_b - \frac{\alpha}{2}[P_t + P_b], \tag{2}$$

Here α is the material's porosity volume fraction, and the porosity content in both the metal and ceramic components is represented by the equation's final term.

The porosity Model 2 presupposed that the porosity is symmetrically distributed around the mid-axis, that its peak is located close to the mid-axis, and that it continuously decreases as it moves away to the top or bottom surface. As shown in Fig. 2, the material distributions for a symmetric model can be implemented by: [93]

$$P(z) = \{[P_t - P_b]V_t + P_b\}\left\{1 - \alpha\cos\left[\pi\frac{z}{h}\right]\right\} \tag{3}$$

As shown in Fig. 2, the third model assumed that porosity concentrates at the bottom surface and reduces upward. As a result, the porous material's thickness was graded as follows [93]:

$$P(z) = \{[P_t - P_b]V_t + P_b\}\left\{1 - \alpha\cos\left[\frac{\pi}{2}\left(\frac{z}{h} + \frac{1}{2}\right)\right]\right\} \tag{4}$$
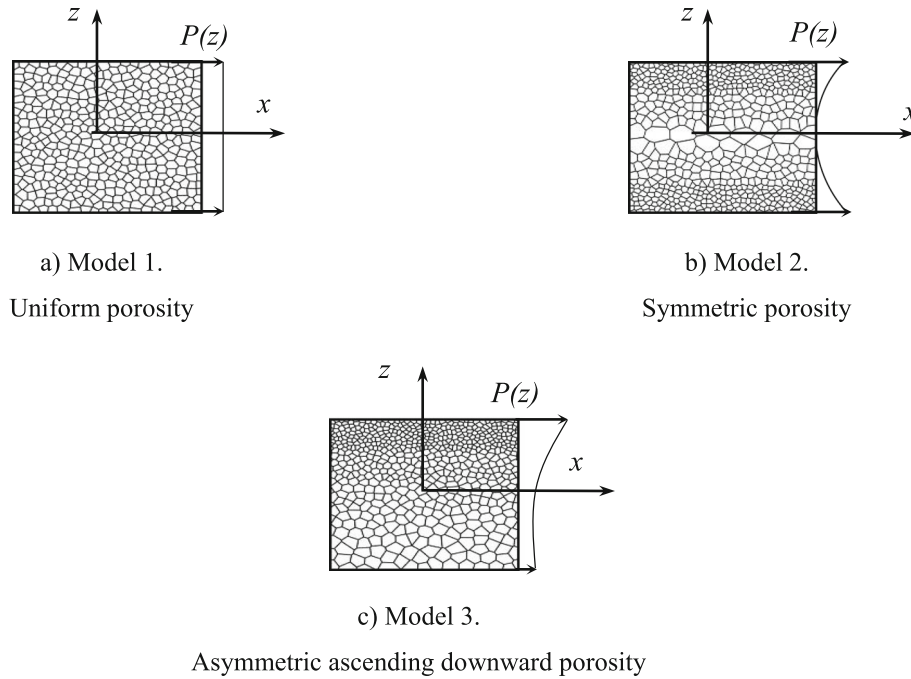
a) Model 1.

Uniform porosity

b) Model 2.

Symmetric porosity

c) Model 3.

Asymmetric ascending downward porosity

Fig. 2 Models for the thickness-based distribution of porosity [94]

2.2 Temperature-dependent material properties

BaTiO$_3$ and CoFe$_2$O$_4$ are the materials used to make the nanosensor beam, and the temperature-dependent material properties for ceramic-based materials are defined as [93, 95, 96]:

$$P = P_0(P_{-1}T^{-1} + 1 + P_1T + P_2T^2 + P_3T^3) \tag{5}$$

P_0, P_{-1}, P_1, P_2, and P_3 are specific coefficients that depend on temperature. The literature lacks research on the temperature-dependent material characteristics of BaTiO$_3$ and CoFe$_2$O$_4$. The expansion coefficients of BaTiO$_3$ and their effective thermal and thermal conductivity values were taken into consideration in this study [97] and [98]. The experimental research derives CoFe$_2$O$_4$'s thermal expansion and thermal conductivity coefficients [99]. For the first time in this study, experimental and numerical studies have been obtained for mechanical properties like Young modulus and Poisson's ratio [100]. These results are shown in Table 1.

The entire FGM beam's temperature is increased to the final temperature T using: assuming the stress-free state at $T_0 = 300$ K for uniform temperature rise

$$\Delta T = T - T_0 \tag{6}$$

The bottom surface temperature is T_b for the linear temperature increase, and it is presumed that the temperature will change linearly along the thickness from T_b to T_t at the top surface. Accordingly, a plane's temperature at z in the thickness is as follows [101]:

$$T(z) = T_b + (T_t - T_b)\left(\frac{h + 2z}{2h}\right) \tag{7a}$$

The steady-state one-dimensional heat transfer equation shown below can be solved when the temperature boundary conditions at the bottom and top of the FGM beam are known, and the temperature can be determined

in the case of nonlinear temperature rise [102]. The temperature at z is as follows for the specified boundary conditions and the variable thermal conductivity coefficient $\kappa(z)$:

$$-\frac{d}{dz}\left(\kappa(z)\frac{dT}{dz}\right) = 0,\ T\left(\frac{h}{2}\right) = T_t,\ T\left(-\frac{h}{2}\right) = T_b,$$

$$T(z) = T_b + \frac{T_t - T_b}{\int_{-\frac{h}{2}}^{\frac{h}{2}}\frac{1}{\kappa(z)}dz}\int_{-\frac{h}{2}}^{z}\frac{1}{\kappa(z)}dz \tag{7b}$$

2.3 Kinematic relations

It is possible to express the displacement field at any point of the nanobeam using advanced shear deformation beam theory:

$$u_1(x, z, t) = u(x, t) - z\frac{\partial w_b}{\partial x} + f(z)\frac{\partial w_s}{\partial x},$$
$$u_2(x, z, t) = 0, u_3(x, z, t) = w_b(x, t) + w_s(x, t). \tag{8}$$

Here w_s, w_b are the shear and bending components of the transverse displacement of a point on the mid-plane of the beam, and u is the displacement of the mid-plane along the x-axis. The shape function $f(z)$ estimates how shear stress is distributed throughout the thickness of the plate [103]. Therefore, there is no requirement to use any shear correction variables. The current theory serves the following purpose:

$$f(z) = z - \sin(\xi z)/\xi. \tag{9}$$

To approximate the quasi-static solution of Maxwell's equation, the electric potential and magnetic potential distributions across the thickness are roughly calculated as follows [103, 104]

$$\Phi(x, z, t) = -\cos(\xi(z))\Phi(x, y, t) + \frac{2(z)}{h}V \tag{10}$$

$$y(x, z, t) = -\cos(\xi(z))\Phi(x, y, t) + \frac{2(z)}{h}\Omega \tag{11}$$

in which $\xi = \pi/h$. Additionally, the nanobeam's external magnetic potential and electric voltage are denoted by V and Ω, respectively. The current beam model's nonzero strains are expressed by

$$\varepsilon_{xx} = \frac{\partial u}{\partial x} - \frac{\partial^2 w_b}{\partial x^2} - f(z)\frac{\partial^2 w_s}{\partial x^2}. \tag{12a}$$

$$\gamma_{xz} = \frac{\partial w_s}{\partial x} \tag{12b}$$

The relationship between electric field (E_x, E_z) and electric potential (Φ) can be calculated using Eq. (10).

$$E_x = -\Phi_x = -\cos\xi(z)\frac{\partial\Phi}{\partial x} \tag{13a}$$

$$E_z = -\Phi_z = -\xi\sin\xi(z)\frac{\partial\Phi}{\partial x} - \frac{2V}{h} \tag{13b}$$

Additionally, Eq. (11) allows for the following expression of the relationship between magnetic field (H_x, H_z) and magnetic potential (Ψ):

$$H_x = -\Psi_x = \cos\xi(z)\frac{\partial\Psi}{\partial x} \tag{14a}$$

$$H_z = -\Psi_z = \xi\sin\xi(z)\Psi - \frac{2\Omega}{h} \tag{14b}$$

The force N^T and moment M^T are defined as follows in response to the rise in temperature:

$$N^T = b\int_{-h/2}^{h/2} C(z, T)\alpha(z, T)\Delta T\,dz \tag{15a}$$

$$M^T = b \int_{-h/2}^{h/2} C(z,T) z \alpha(z,T) \Delta T \, dz \tag{15b}$$

The motion equation can be derived using an extension of Hamilton's principle by:

$$\int_0^t \delta(\Pi_s - \Pi_k + \Pi_w) dt = 0 \tag{16}$$

Here, Π_s stands for strain energy, Π_w is work produced by outside forces, and Π_k is kinetic energy. The following is an example of the virtual variation of strain energy:

$$\delta \Pi_s = \int_V \sigma_{lj} \delta_{lj} dV = \int_V (\sigma_x \delta \varepsilon_x + \sigma_{xz} \delta y_{xz} - D_x \delta E_x - D_z \delta E_z - B_x \delta h_x - B_z \delta h_z) dV \tag{17}$$

Equation (17) with Eqs. (10) and (12) substituted produces

$$\delta \Pi_s = \int_0^l \left[N_x \frac{\partial \delta u}{\partial x} - M_x^b \frac{\partial^2 \delta w_b}{\partial x^2} - M_x^s \frac{\partial^2 \delta w_s}{\partial x^2} - Q_{xz} \frac{\partial \delta w_s}{\partial x^2} \right] dx$$

$$+ \int_0^l \int_{h/2}^{-h/2} \left[D_x \cos(\xi z) \delta \left(\frac{\partial \Phi}{\partial x} \right) + D_z \sin \xi (\xi z) \delta \Phi - B_x \cos(\xi z) \delta \left(\frac{\partial \Psi}{\partial x} \right) + B_z \sin \xi (\xi z) \delta \Psi \right] dz dx \tag{18}$$

which expresses the variables at the final expression as:

$$\left(N_i, M_i^b, M_i^s \right) = \int_A (1, z, f) \sigma_i dA, i = (x, y, xy) \tag{19}$$

$$Q_i = \int_A g \sigma_i dA, i = (xz, yz) \tag{20}$$

The first type of work brought about by applied forces can be summed up as follows:

$$\delta \Pi_w = \int_0^l \left(N_x^0 \frac{\partial (w_b + w_s)}{\partial x} \frac{\partial \delta (w_b + w_s)}{\partial x} + q \delta (w_b + w_s) \right) dx \tag{21}$$

Here q is the external transverse load and N_x^0 are applied loads in plane.
The current plate model's first variational of virtual kinetic energy has the following form:

$$\delta k = \int_0^l \left[l_0 \left(\frac{\partial u}{\partial t} \frac{\partial \delta u}{\partial t} + \frac{\partial (w_b + w_s)}{\partial t} \frac{\partial \delta u (w_b + w_s)}{\partial t} \right) - I_1 \left(\frac{\partial u}{\partial t} \frac{\partial \delta w_b}{\partial x \partial t} + \frac{\partial w_b}{\partial x \partial t} \frac{\partial \delta u}{\partial t} \right) \right.$$

$$- J_1 \left(\frac{\partial u}{\partial t} \frac{\partial \delta w_s}{\partial x \partial t} + \frac{\partial w_s}{\partial x \partial t} \frac{\partial \delta u}{\partial t} \right) + J_2 \left(\frac{\partial w_b}{\partial x \partial t} \frac{\partial \delta w_b}{\partial x \partial t} \right)$$

$$\left. + K_2 \left(\frac{\partial w_s}{\partial x \partial t} \frac{\partial \delta w_s}{\partial x \partial t} \right) + J_2 \left(\frac{\partial w_b}{\partial x \partial t} \frac{\partial \delta w_s}{\partial x \partial t} + \frac{\partial w_s}{\partial x \partial t} \frac{\partial \delta w_b}{\partial x \partial t} \right) \right] dA dX \tag{22}$$

where mass inertia, defined as I_0, I_1, J_1, I_2, J_2, and K_2, is:

$$(I_0, I_1, J_1, I_2, J_2, K_2) = \int_{h/2}^{-h/2} \left(1, z, f, z^2, zf, f^2 \right) \rho(z) dz \tag{23}$$

When the coefficients of δu, δw_b, δw_s, $\delta \Phi$, and $\delta \Psi$ are equal to zero, they are then inserted into Eq. (16), which results in the following equations:

$$\frac{\partial N_x}{\partial x} = I_0 \frac{\partial^2 u}{\partial t^2} - I_1 \frac{\partial^3 w_b}{\partial x \partial t^2} - J_1 \frac{\partial^3 w_s}{\partial x \partial t^2} \tag{24}$$

$$\frac{\partial^2 M_x^b}{\partial x^2} - \left(N^E + N^H\right)\nabla^2(w_b + w_s) = I_0 \frac{\partial^2 (w_b + w_s)}{\partial t^2} + I_1\left(\frac{\partial^3 u}{\partial x \partial t^2}\right) - I_2\nabla^2\left(\frac{\partial^2 w_b}{\partial t^2}\right) - J_2\nabla^2\left(\frac{\partial^2 w_s}{\partial t^2}\right) + q \tag{25}$$

$$\frac{\partial^2 M_x^s}{\partial x^2} + \frac{\partial Q_{xz}}{\partial x} - \left(N^E + N^H + N^T\right)\nabla^2(w_b + w_s) = J_0 \frac{\partial^2 (w_b + w_s)}{\partial t^2} + J_1\left(\frac{\partial^3 u}{\partial x \partial t^2}\right)$$
$$- J_2\nabla^2\left(\frac{\partial^2 w_b}{\partial t^2}\right) - K_2\nabla^2\left(\frac{\partial^2 w_s}{\partial t^2}\right) + q \tag{26}$$

$$\int_{h/2}^{-h/2} \left(\cos(\xi z)\frac{\partial D_x}{\partial x} + \xi\sin(\xi z)D_z\right)dz = 0 \tag{27}$$

$$\int_{h/2}^{-h/2} \left(\cos(\xi z)\frac{\partial B_x}{\partial x} + \xi\sin(\xi z)B_z\right)dz = 0 \tag{28}$$

The total stress at any point is defined as follows [7] based on the NSGT:

$$\sigma_i^t = \sigma_i^c - \nabla^2\sigma_i^h, i = xx, xz. \tag{29}$$

$$\sigma_{i,j}^c = \int_V \alpha_0(\boldsymbol{x'}, \boldsymbol{x}, e_0 a)\boldsymbol{C}_{i,j} : \varepsilon_{i,j'}(\boldsymbol{x'})dV(\boldsymbol{x'}),$$

$$\sigma_{i,j}^h = l_m^2 \int_V \alpha_1(\boldsymbol{x'}, \boldsymbol{x}, e_1 a)\boldsymbol{C}_{i,j} : \nabla\varepsilon_{i,j'}(\boldsymbol{x'})dV(\boldsymbol{x'}). \tag{30}$$

Here ∇ stands for the Laplacian operator and σ_i^c and σ_i^h are the higher-order stresses, and $e_0 a$ and $e_1 a$ are the nonlocality coefficients, l_m is the material length scale parameter, and α_1 and α_0 are the higher-order and classical nonlocal kernel functions, respectively [13]. The following constitutive equations for the total normal and shear stress are derived as [7] using the linear differential operator, assuming $e = e_0 = e_1$ and the nonlocal functions $\alpha_0(\boldsymbol{x'}, \boldsymbol{x}, e_0 a)$ and $\alpha_1(\boldsymbol{x'}, \boldsymbol{x}, e_1 a)$ are in the frame of the assumptions of [13].

$$\left[1 - (ea)^2\nabla^2\right]\sigma_{i,j}^t = \left[1 - l_m^2\nabla^2\right]C_{i,j}(z)\varepsilon_{i,j}, i, j = xx, xz. \tag{31}$$

Here the strains and stiffnesses are $C_{i,j}(z)$ and $\varepsilon_{i,j}$. Theory of nonlocal strain gradient elasticity for magnetoelastic materials Eringen's nonlocal theory [3, 13] introduces the stress state as a function of the strains at all other points in the body. Strain gradient plasticity [105] presents the stiffness-enhancing effect with a material size parameter. The nonlocal strain gradient elasticity has finally been proposed [7, 21, 106], combining Eringen's integral elasticity and strain gradient elasticity in one model. Therefore, the following expression gives the fundamental relationships with zero body force for a nonlocal magneto-electro-elastic structural element.

$$\sigma_{i,j} = \int_v \alpha\left(\left|x'-x\right|, \tau\right)\left[C_{ijkl}\varepsilon_k\left(x'\right) - e_{mij}E_m\left(x'\right) - q_{mij}H_n\left(x'\right)\right]dv\left(x'\right) \tag{32}$$

$$D_i = \int_v \alpha\left(\left|x'-x\right|, \tau\right)\left[e_{ikl}\varepsilon_{kl} + s_{im}E_m\left(x'\right) - d_{in}H_n\left(x'\right)\right]dv\left(x'\right) \tag{33}$$

$$B_i = \int_v \alpha\left(\left|x'-x\right|, \tau\right)\left[q_{ikl}\varepsilon_{kl}\left(x'\right) + d_{im}E_m\left(x'\right) + \chi_{in}H_n\left(x'\right)\right]dv\left(x'\right) \tag{34}$$

The terms strain, stress, electric displacement, electric field components, magnetic field, and magnetic induction components are denoted by the letters $\varepsilon_{i,j}$, $\sigma_{i,j}$, D_i, E_i, H_i, and B_i, respectively. Piezoelectric, elastic, dielectric, piezomagnetic, magnetic, and magnetoelectric constants are denoted by the letters e_{mij}, C_{ijkl}, s_{im}, q_{mij}, χ_{in}, and d_{im}. The nonlocal kernel function is $\alpha\left(\left|x'-x\right|, \tau\right)$, and the Euclidean distance is $\left|x'-x\right|$. Lastly, an equivalent differential form for the constitutive relations of a MEE solid is as follows [103].

Elastic strain gradient included:

$$\sigma_{i,j} - (e_0 a)^2 \nabla^2 \sigma_{i,j} = \left(1 - l_m^2 \nabla^2\right)\left[C_{ijkl}\varepsilon_k - e_{mij}E_m - q_{mij}H_n\right] \tag{35}$$

$$D_i - (e_0 a)^2 \nabla^2 d_i = \left(1 - l_m^2 \nabla^2\right)[e_{ikl}\varepsilon_{ikl} + s_{im}E_m + d_{in}H_n] \tag{36}$$

$$B_i - (e_0 a)^2 \nabla^2 B_i = \left(1 - l_m^2 \nabla^2\right)[q_{ikl}\varepsilon_k + d_{im}E_m + \chi_{in}H_n] \tag{37}$$

Here ∇^2 denotes the Laplacian operator, $e_0 a$ denotes a nonlocal variable, and l_m denotes the material size parameter, both of which introduce the small-size effects. The stress–strain relations can be formulated as follows:

$$\left(1 - (e_0 a)^2 \nabla^2\right)\sigma_{xx} = \left(1 - l_m^2 \nabla^2\right)\left[C_{11}\varepsilon_{xx} - e_{31}E_z - q_{31}H_z\right] \tag{38}$$

$$\left(1 - (e_0 a)^2 \nabla^2\right)\sigma_{xz} = \left(1 - l_m^2 \nabla^2\right)\left[C_{55}\gamma_{xz} - e_{15}E_x - q_{15}H_x\right] \tag{39}$$

$$\left(1 - (e_0 a)^2 \nabla^2\right)D_x = \left(1 - l_m^2 \nabla^2\right)\left[e_{15}\gamma_{xz} + s_{11}E_x + d_{11}H_x\right] \tag{40}$$

$$\left(1 - (e_0 a)^2 \nabla^2\right)D_z = \left(1 - l_m^2 \nabla^2\right)\left[e_{31}\varepsilon_{xx} + s_{33}E_z + d_{33}H_z\right] \tag{41}$$

$$\left(1 - (e_0 a)^2 \nabla^2\right)B_x = \left(1 - l_m^2 \nabla^2\right)\left[q_{15}\gamma_{xz} + d_{11}E_x + x_{11}H_x\right] \tag{42}$$

$$\left(1 - (e_0 a)^2 \nabla^2\right)B_z = \left(1 - l_m^2 \nabla^2\right)\left[q_{31}\varepsilon_{xx} + d_{33}E_z + x_{33}H_x\right] \tag{43}$$

For a more accurate FGM beam model, the NSGT and integrating Eqs. (38)–(43) over the cross section area yield the following relations as:

$$\left(1 - (e_0 a)^2 \frac{\partial^2}{\partial x^2}\right)N_x = \left(1 + l_m^2 \frac{\partial^2}{\partial x^2}\right)\left[A_{11}\frac{\partial u}{\partial x} - B_{11}\frac{\partial^2 w_b}{\partial x^2} - B_{11}^s\frac{\partial^2 w_s}{\partial x^2} + A_{31}^e\Phi + A_{31}^m\Psi - N_x^E - N_x^H\right]. \tag{44}$$

$$\left(1 - (e_0 a)^2 \frac{\partial^2}{\partial x^2}\right)M_x^b = \left(1 + l_m^2 \frac{\partial^2}{\partial x^2}\right)\left[B_{11}\frac{\partial u}{\partial x} - D_{11}\frac{\partial^2 w_b}{\partial x^2} - D_{11}^s\frac{\partial^2 w_s}{\partial x^2} + E_{31}^e\Phi + E_{31}^m\Psi - M_{bx}^E - M_{bx}^H\right] \tag{45}$$

$$\left(1 - (e_0 a)^2 \frac{\partial^2}{\partial x^2}\right)M_x^s = \left(1 + l_m^2 \frac{\partial^2}{\partial x^2}\right)\left[B_{11}^s\frac{\partial u}{\partial x} - D_{11}^s\frac{\partial^2 w_b}{\partial x^2} - H_{11}^s\frac{\partial^2 w_s}{\partial x^2} + F_{31}^e\Phi + F_{31}^m\Psi - M_{sx}^E - M_{sx}^H\right] \tag{46}$$

$$\left(1 - (e_0 a)^2 \frac{\partial^2}{\partial x^2}\right)Q_{xz} = \left(1 + l_m^2 \frac{\partial^2}{\partial x^2}\right)\left[A_{55}^s\frac{\partial w_s}{\partial x} - A_{15}^e\frac{\partial \Phi}{\partial x} - A_{15}^m\frac{\partial \Psi}{\partial x}\right] \tag{47}$$

$$\int_{h/2}^{-h/2}\left(1 - (e_0 a)^2 \frac{\partial^2}{\partial x^2}\right)D_x \cos(\xi z)dz = \left(1 + l_m^2 \frac{\partial^2}{\partial x^2}\right)\left[E_{15}^e\frac{\partial w_s}{\partial x} + F_{11}^e\frac{\partial \Phi}{\partial x} + F_{11}^m\frac{\partial \Psi}{\partial x}\right] \tag{48}$$

$$\int_{h/2}^{-h/2}\left(1 - (e_0 a)^2 \frac{\partial^2}{\partial x^2}\right)D_z \xi \sin(\xi z)dz$$

$$= \left(1 + l_m^2 \frac{\partial^2}{\partial x^2}\right)\left[A_{31}^e\left(\frac{\partial u}{\partial x}\right) - E_{31}^e\nabla^2 w_b - F_{31}^e\nabla^2 w_s - F_{33}^e\Phi - F_{33}^m\Psi\right] \tag{49}$$

$$\int_{h/2}^{-h/2}\left(1 - (e_0 a)^2 \frac{\partial^2}{\partial x^2}\right)B_x \cos\xi(\xi z)dz = \left(1 + l_m^2 \frac{\partial^2}{\partial x^2}\right)\left[E_{15}^m\frac{\partial w_s}{\partial x} + F_{11}^m\frac{\partial \Psi}{\partial x} + X_{11}^m\frac{\partial \Psi}{\partial x}\right] \tag{50}$$

$$\int_{h/2}^{-h/2}\left(1 - (e_0 a)^2 \frac{\partial^2}{\partial x^2}\right)B_z \sin\xi(\xi z)dz = \left(1 + l_m^2 \frac{\partial^2}{\partial x^2}\right)\left[A_{15}^m\left(\frac{\partial u}{\partial x}\right) - E_{31}^m\nabla^2 w_b - F_{33}^m\Psi - x_{33}^m\Psi\right] \tag{51}$$

with the following definitions applying to the cross-sectional rigidities:

$$\left\{A_{11}, B_{11}, B_{11}^s, D_{11}, H_{11}^s\right\} = \int\limits_{h/2}^{-h/2} \{c_{11}\}\left(1, z, f, z^2, zf, f^2\right)dz \tag{52}$$

$$\left\{A_{31}^e, E_{31}^e, F_{31}^e\right\} = \int\limits_{h/2}^{-h/2} e_{31}\xi\sin\left(\xi z\right)(1, z, f)dz \tag{53}$$

$$\left\{A_{31}^m, E_{31}^m, F_{31}^m\right\} = \int\limits_{h/2}^{-h/2} q_{31}\xi\sin\left(\xi z\right)(1, z, f)dz \tag{54}$$

$$\left\{A_{15}^e, E_{15}^e\right\} = \int\limits_{h/2}^{-h/2} e_{15}\cos\left(\xi z\right)(1, g)dz \tag{55}$$

$$\left\{A_{15}^m, E_{15}^m\right\} = \int\limits_{h/2}^{-h/2} q_{15}\cos\left(\xi z\right)(1, g)dz \tag{56}$$

$$\left\{F_{15}^e, F_{33}^e\right\} = \int\limits_{h/2}^{-h/2} \left\{s_{11}\cos^2(\xi z), s_{33}\xi^2\sin^2(\xi z)\right\}dz \tag{57}$$

$$\left\{F_{11}^m, F_{33}^m\right\} = \int\limits_{h/2}^{-h/2} \left\{d_{11}\cos^2(\xi z), d_{33}\xi^2 sin^2(\xi z)\right\}dz \tag{58}$$

$$\left\{x_{11}^m, x_{33}^m\right\} = \int\limits_{h/2}^{-h/2} \left\{x_{11}\cos^2(\xi z), x_{33}\xi^2\sin^2(\xi z)\right\}dz \tag{59}$$

$$A_{55}^s = \int\limits_{h/2}^{-h/2} c_{55}g^2dz \tag{60}$$

The following definitions apply to the normal forces and moments resulting from the magnetoelectric field in Eqs. (38)– (43).

$$N_x^E = -\int\limits_{h/2}^{-h/2} e_{31}\frac{2V}{h}dz, N_x^H = -\int\limits_{h/2}^{-h/2} q_{31}\frac{2\Omega}{h}dz \tag{61}$$

$$M_{bx}^E = -\int\limits_{h/2}^{-h/2} e_{31}\frac{2V}{h}zdz, M_{bx}^H = -\int\limits_{h/2}^{-h/2} q_{31}\frac{2\Omega}{h}zdz \tag{62}$$

$$M_{sx}^E = -\int\limits_{h/2}^{-h/2} e_{31}\frac{2V}{h}f(z)dz, M_{sx}^H = -\int\limits_{h/2}^{-h/2} q_{31}\frac{2\Omega}{h}f(z)dz \tag{63}$$

Equations (44)–(51) can be substituted into Eqs. (24)–(28) to derive the refined nanobeam's governing equations in terms of displacement:

$$\left(1 + l_m^2\frac{\partial^2}{\partial x^2}\right)\left[A_{11}\frac{\partial^2 u}{\partial x^2} - B_{11}\frac{\partial^3 w_b}{\partial x^3} - B_{11}^s\frac{\partial^3 w_s}{\partial x^3} + A_{31}^e\frac{\partial\Phi}{\partial x} + A_{31}^m\frac{\partial\Psi}{\partial x}\right]$$
$$+ \left(1 + (e_0a)^2\frac{\partial^2}{\partial x^2}\right)\left(-I_0\frac{\partial^2 u}{\partial x^2} + I_1\frac{\partial^3 w_b}{\partial x\partial t^2} + J_1\frac{\partial^3 w_s}{\partial x\partial t^2}+\right) = 0 \tag{64}$$

Table 2 Boundary conditions and the admissible shape function

	Boundary Conditions		Function X_m
	At $x = 0$	At $x = L$	
S–S (Simply supported)	$X_n(0) = 0$ $X_n''(0) = 0$	$X_n(L)=0$ $X_n''(L) = 0$	$\sin\left(\frac{n\pi}{L}x\right)$
C-S (Clamped-Simply)	$X_n(0) = 0$ $X_n'(0) = 0$	$X_n(L)=0$ $X_n''(L) = 0$	$\sin\left(\frac{n\pi}{L}x\right)\left[\cos\left(\frac{n\pi}{L}x\right) - 1\right]$
C–C (Clamped–Clamped)	$X_n(0) = 0$ $X_n'(0) = 0$	$X_n(L)=0$ $X_n'(L) = 0$	$\sin^2\left(\frac{n\pi}{L}x\right)$
C–F (Clamped-Free)	$X_n(0) = 0$ $X_n'(0) = 0$	$X_n'''(L)=0$	$\left(1 - \cos(n - 0.5)\frac{\pi}{L}x\right)$

$$\left(1 + l_m^2 \frac{\partial^2}{\partial x^2}\right)\left[B_{11}\frac{\partial^3 u}{\partial x^3} - D_{11}\frac{\partial^4 w_b}{\partial x^4} - D_{11}^s\frac{\partial^4 w_s}{\partial x^4} + E_{31}^e\left(\frac{\partial^2 \Phi}{\partial x^2}\right)\right.$$

$$-A_{15}^e\left(\frac{\partial^2 \Phi}{\partial x^2}\right) + E_{31}^m\left(\frac{\partial^2 \Psi}{\partial x^2}\right) - A_{15}^m\left(\frac{\partial^2 \Psi}{\partial x^2}\right)\right]$$

$$+ \left(1 + (e_0 a)^2 \frac{\partial^2}{\partial x^2}\right)\left[-I_1\frac{\partial^3 u}{\partial x \partial t^2} - I_0\frac{\partial^2(w_b + w_s)}{\partial t^2} + I_2\frac{\partial^4 w_b}{\partial x^2 \partial t^2}\right.$$

$$\left. + J_2\frac{\partial^4 w_s}{\partial x^2 \partial t^2} - \left(N^E + N^H + N^T\right)\left(\frac{\partial^2(w_b + w_s)}{\partial x^2}\right)\right] = 0 \tag{65}$$

$$\left(1 + l_m^2 \frac{\partial^2}{\partial x^2}\right)\left[B_{11}^s\frac{\partial^3 u}{\partial x^3} - D_{11}^s\frac{\partial^4 w_b}{\partial x^4} - H_{11}^s\frac{\partial^4 w_s}{\partial x^4} + A_{55}^s\frac{\partial^2 w_s}{\partial x^2} - A_{15}^e\left(\frac{\partial^2 \Phi}{\partial x^2}\right)\right.$$

$$\left. + F_{31}^e\left(\frac{\partial^2 \Phi}{\partial x^2}\right) + F_{31}^m\left(\frac{\partial^2 \Psi}{\partial x^2}\right) - A_{15}^m\left(\frac{\partial^2 \Psi}{\partial x^2}\right)\right]$$

$$+ \left(1 + (e_0 a)^2 \frac{\partial^2}{\partial x^2}\right)\left[-I_0\frac{\partial^2(w_b + w_s)}{\partial t^2} - J_1\frac{\partial^3 u}{\partial x \partial t^2} + J_2\left(\frac{\partial^4 w_b}{\partial x^2 \partial t^2}\right)\right.$$

$$\left. + K_2\left(\frac{\partial^4 w_b}{\partial x^2 \partial t^2}\right) - \left(N^E + N^H + N^T\right)\left(\frac{\partial^2(w_b + w_s)}{\partial x^2}\right)\right] = 0 \tag{66}$$

$$\left(1 + l_m^2 \frac{\partial^2}{\partial x^2}\right)\left[A_{31}^e\left(\frac{\partial u}{\partial x}\right) - E_{31}^e\left(\frac{\partial^2 w_b}{\partial x^2}\right) - \left(F_{31}^e - E_{15}^e\right)\left(\frac{\partial^2 w_s}{\partial x^2}\right)\right.$$

$$\left. + F_{11}^e\left(\frac{\partial^2 \Phi}{\partial x^2}\right) + F_{11}^m\left(\frac{\partial^2 \Psi}{\partial x^2}\right) - F_{33}^e\Phi - F_{33}^m\Psi\right] = 0 \tag{67}$$

$$\left(1 + l_m^2 \frac{\partial^2}{\partial x^2}\right)\left[A_{31}^m\left(\frac{\partial u}{\partial x}\right) - E_{31}^m\left(\frac{\partial^2 w_b}{\partial x^2}\right) - \left(F_{31}^m - E_{15}^m\right)\left(\frac{\partial^2 w_s}{\partial x^2}\right)\right.$$

$$\left. + F_{11}^m\left(\frac{\partial^2 \Phi}{\partial x^2}\right) + X_{11}^m\left(\frac{\partial^2 \Psi}{\partial x^2}\right) - F_{33}^m\Phi - X_{33}^m\Psi\right] = 0 \tag{68}$$

$$N_x^0 = N^E + N^H$$

$$N^E = -\int\limits_{h/2}^{-h/2} e_{31}\frac{2V}{h}dz, N^H = -\int\limits_{h/2}^{-h/2} q_{31}\frac{2\Omega}{h}dz \tag{69}$$

3 Solutions of the problem

For the solution of the motion Eqs. in (64–68), one can use the Navier's methods in Eqs. (72–76) adapting the desired boundary conditions in Table 2.

The boundary conditions for simply supported (S):

$$w_b = w_s = N_x = M_x = 0 \, at = 0, L \tag{70}$$

For clamped (C):

$$u = w_b = w_s = 0 \, at \, x = 0, L \tag{71}$$

The other boundary conditions and the related displacement functions are presented in Table 2.

The displacement quantities are given in the form shown below to satisfy the boundary conditions mentioned above:

$$u = \sum_{n=1}^{\infty} U_n \frac{\partial X_n(x)}{\partial_x} e^{i\omega_n t} \tag{72}$$

$$w_b = \sum_{n=1}^{\infty} W_{bn} X_n(x) e^{i\omega_n t} \tag{73}$$

$$w_s = \sum_{n=1}^{\infty} W_{sn} X_n(x) e^{i\omega_n t} \tag{74}$$

$$\Phi = \sum_{n=1}^{\infty} \phi_n X_n(x) e^{i\omega_n t} \tag{75}$$

$$\Psi = \sum_{n=1}^{\infty} Y_n X_n(x) e^{i\omega_n t} \tag{76}$$

For the trigonometric solution of Eqs. (64–68), the assumed displacement Eqs. (72–76) are used for the desired boundary conditions given in Table 2. Finally, the eigenvalue equations in Appendix (A.1–A.5) for the displacements U_n, W_{bn}, W_{sn}, and electric and magnetic potentials Φ_n and Y_n are derived, and the equations can be shortened in the following matrix equation as follows:

$$\left\{ [K] - [M]\omega^2 \right\} \begin{Bmatrix} U_n \\ W_{bn} \\ W_{sn} \\ \phi_n \\ Y_n \end{Bmatrix} = 0 \tag{77}$$

4 Numerical results and verification

4.1 Numerical validation

This research examined the BaTiO$_3$, and CoFe$_2$O$_4$ porous FG nanobeam's free vibration behavior. In Table 3, the material's mechanical and physical characteristics are listed. The numerical analyses considered a simply supported beam with dimensions of length $L = 10$ nm, width b, and thickness h (and $h = L/10$). The bottom and top surfaces of the nanobeam are made of BaTiO$_3$ and CoFe$_2$O$_4$, respectively. The material composition changes functionally with thickness in accordance with a power-law, as shown in Eq. (1). The material power-law exponent is represented by the parameter p. When $p = 0$, the beam is entirely made of the material on the upper side (BaTiO$_3$), while when p, the material on the lower side makes up the entire beam. For instance, the composition of the nanobeam material at $p = 1$ is 50% BaTiO$_3$ and the rest CoFe$_2$O$_4$. While CoFe$_2$O$_4$ makes up the remaining part of the nanobeam material when $p = 5$, BaTiO$_3$ makes up about 83.33 percent of it. Although the total amounts are equal, the distribution law dictates that the BaTiO$_3$ ratio will decrease from the bottom surface and increase through the thickness until only CoFe$_2$O$_4$ remains. The CoFe$_2$O$_4$ ratio is 100%, and the BaTiO$_3$ ratio is 0% on the upper surface. In that case, the eigenvalue equation is used to determine the system's natural frequencies (Eq. 78). The following equation defines the dimensionless frequencies in this situation:

$$\lambda_i = \omega_i L^2 \sqrt{\rho_t A / C_{t11} I}, \tag{78}$$

Table 3 CoFe$_2$O$_4$ and BaTiO$_3$'s magnetic, piezoelectric, electro, and thermal characteristics

		CoFe$_2$O$_4$	BaTiO$_3$
C_{11}	[GPa]	286	166
C_{22}		286	166
C_{33}		269.5	162
C_{12}		173	77
C_{13}		170.5	78
C_{23}		170.5	78
C_{44}		45.3	43
C_{55}		45.3	43
C_{66}		56.5	44.5
e_{31}	[C/m^2]	0	− 4.4
e_{32}		0	− 4.4
e_{33}		0	18.6
q_{31}	[N/A.m]	580.3	0
q_{32}		580.3	0
q_{33}		699.7	0
ξ_{11}	[10^{-9}C^2/N.m^2]	0.08	11.2
ξ_{22}		0.08	11.2
ξ_{33}		0.093	12.6
$\zeta_{11} = \zeta_{22} = \zeta_{33}$	[s/m]	0	0
χ_{11}	[10^{-6} N.s^2/C]	− 590	5
χ_{22}		− 590	5
χ_{33}		157	10
$p_{11} = p_{22}$	[10^{-7}C/m^{2}K]	0	0
p_{33}		0	− 11.4
$\lambda_{11} = \lambda_{22}$	[10^{-5}Wb/m^{2}K]	0	0
λ_{33}		− 36.2	0
$\alpha_1 = \alpha_2$	[10^{-6} K^{-1}]	10	15.8
ρ	[kg/m^3]	5800	5300

Table 4 Dimensionless frequency comparison of magneto-electro-thermo-elastic FG nanobeams

Voltage		$p = 0.2$	$p = 1$	$p = 5$	$p = 0.2$	$p = 1$	$p = 5$
V = − 5	[107]	8.08984	7.91790	8.03872	9.84516	9.00077	8.39941
	[103]	8.08985	7.91806	8.03900	9.84516	9.00091	8.39968
	Present	8.08982	7.91796	8.03908	9.84522	9.00088	8.39962
V = 0	[107]	7.94094	7.46642	7.30630	9.72317	8.60629	7.70137
	[103]	7.94095	7.46659	7.30661	9.72318	8.60644	7.70166
	Present	7.94094	7.46648	7.30652	9.72314	8.60636	7.70159
V = + 5	[107]	7.78919	6.98583	6.49177	9.59964	8.19284	6.93341
	[103]	7.78920	6.98601	6.49212	9.59964	8.19299	6.93373
	Present	7.78920	6.98592	6.49192	9.59961	8.19288	6.93361

Table 5 Comparisons of the dimensionless frequency λ_1 for the L = 10 nm, h = 0.1 nm FGM nanobeam for different material grading indices and nonlocal parameters

| $(e_0 a)^2$ nm^2	$p = 0$			$p = 0.2$			$p = 5$		
	Present	[108]	[110]	Present	[108]	[110]	Present	[108]	[110]
0	9.86326	9.8631	9.86315	8.68948	8.6895	8.68954	5.93875	5.9389	5.93894
1	9.40966	9.4097	9.40973	8.29001	8.2901	8.29007	5.66584	5.6659	5.66592
2	9.01339	9.0136	9.01358	7.94116	7.9411	7.94106	5.42751	5.4274	5.42739
3	8.66353	8.6636	8.66360	7.63259	7.6327	7.63272	5.21671	5.2166	5.21665
4	8.35129	8.3515	8.35146	7.35753	7.3577	7.35772	5.02863	5.0287	5.02869
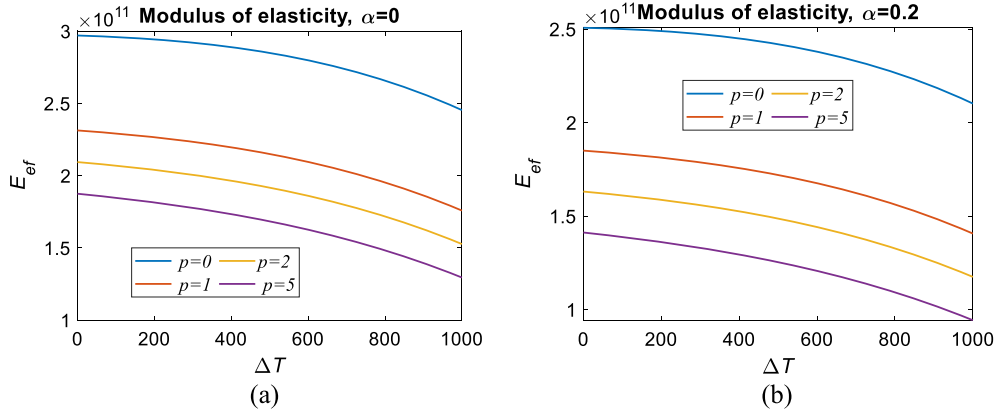
Fig. 3 Comparison of the elasticity modulus of the nanobeam depending on the uniform porosity (Model 1, $\alpha = 0$, and 0.2), four different material grading indices ($p = 0, 1, 2$, and 5), and the ΔT in the range 0–1000 K, where the material grading index is $p = 0$, the entire nanobeam is composed of $CoFe_2O_4$
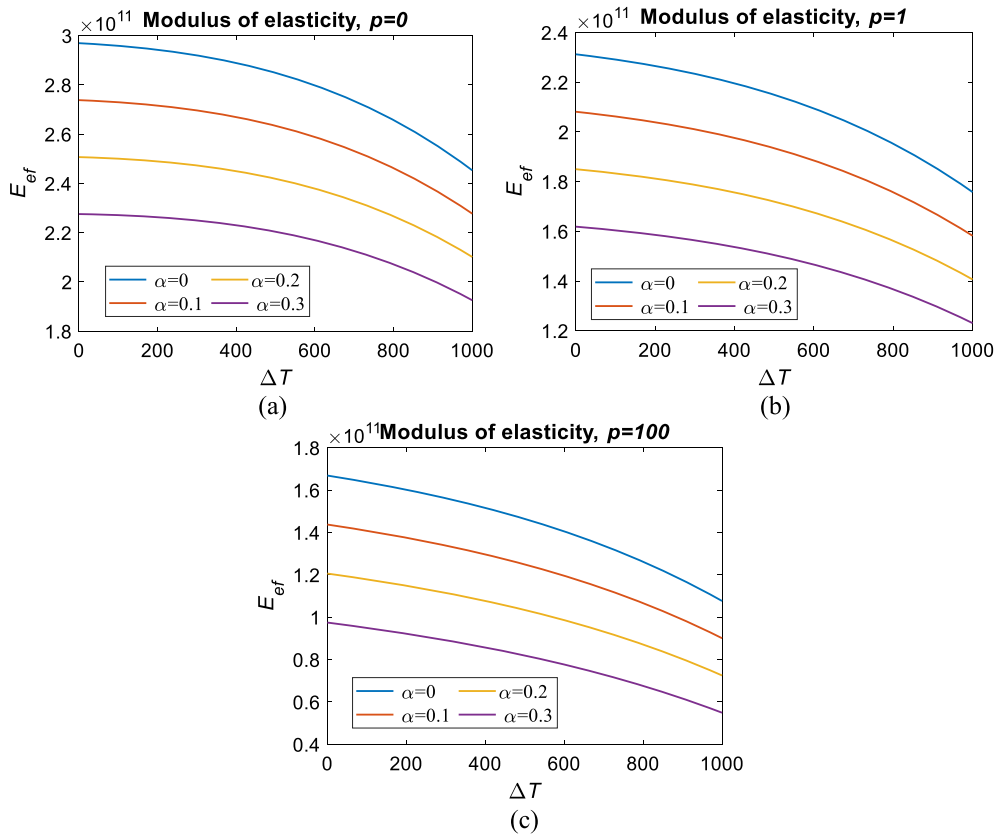

Fig. 4 Comparison of the elasticity modulus of the nanobeam depending on the four different uniform porosities ($\alpha = 0, 0.1$, 0.2, and 0.3), material grading index p, and the ΔT in the range 0–1000 K, a) At the material grading index is $p = 0$, the entire nanobeam is composed of $CoFe_2O_4$ b) At $p = 1$ the nanobeam is composed of 50% $CoFe_2O_4$ and 50% $BaTiO_3$ c) At $p = 100$, the material composition is of 99% $BaTiO_3$
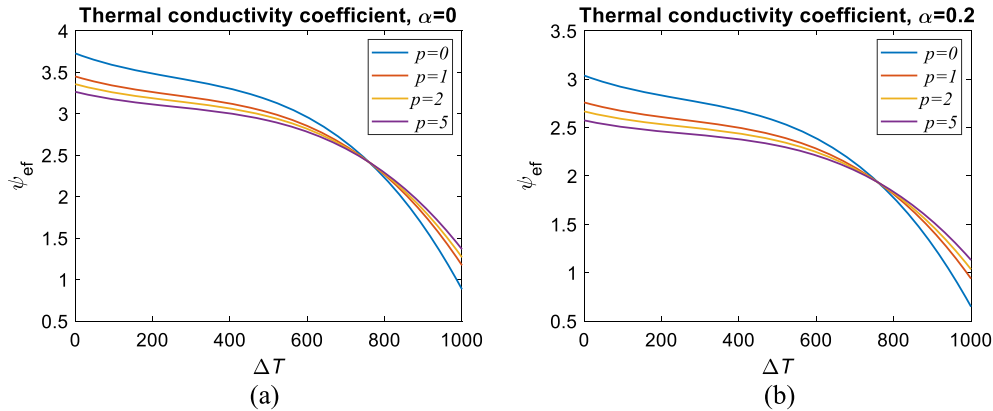
Fig. 5 Comparison of the thermal conductivity coefficient of the nanobeam depending on the uniform porosity (Model 1, $\alpha = 0$, and 0.2), four different material grading indices ($p = 0, 1, 2,$ and 5), and the ΔT in the range 0–1000 K, where the material grading index is $p = 0$, the entire nanobeam is composed of $CoFe_2O_4$

Here a is the beam's width, h is its thickness, and ρ_t and C_{t11} are pure $CoFe_2O_4$'s specific gravity and elastic modulus, respectively.

A comparison study between the current method and the analytical methods described in the literature is carried out using a simply supported FGM beam made of $BaTiO_3$ and $CoFe_2O_4$. Table 4 compares the dimensionless fundamental frequency λ_1 calculated using Eq. (46), using the same material properties [103, 107], for the same conditions. As shown in Table 2, the results of the current method and the analytical methods [103, 107] are in good agreement.

Comparing the obtained dimensionless frequencies $\lambda_i = \omega_i L^2 \sqrt{\rho_c A / E_c I}$ of a FGM nanobeam with $L = 10$ nm, $h = L/10$, and $b = h$ to those reported in the literature for the same prior material properties (Table 3), taking into account the nonlocality effect, Table 5 shows the comparison's findings, and it can be seen that the outcomes of the present method for the nonlocality effect are in strong agreement with those presented by [108, 109].

4.2 Temperature-dependent material properties of the MEE nanobeam

Using the temperature-dependent mechanical properties such as the thermal expansion coefficient, thermal conductivity coefficient, and the modulus of elasticity given in Table 1, the nanobeam effective material properties were calculated according to the porosity ratio α, the material grading index p, and the uniform distribution function, which determine the material composition of the nanobeam, and the results are given in Figs. (3–8).

The effective elasticity modulus of the nanobeam is given for four different material grading indices $p = 0, 1, 2, 3$, and for porosity volume fraction $\alpha = 0$ in Fig. 3a and in Fig. 3b for porosity volume fraction $\alpha = 0.2$. In Fig. 4a, p = 0, that is, the porosity ratios of the effective elasticity modulus of the nanobeam consisting of pure $CoFe_2O_4$ are given for $\alpha = 0, 0.1, 0.2$ and 0.3, while in Fig. 4b, p = 1, that is, the nanobeam composed of 50% $BaTiO_3$ and 50% $CoFe_2O_4$. In Fig. 4c, the temperature-dependent variation of the effective modulus of elasticity of the nanobeam, which consists of approximately 99.1% pure $BaTiO_3$ at $p = 100$, is presented according to the same porosity ratios.

According to Fig. 3, the effective modulus of elasticity of the nanobeam decreases as the temperature difference and the material grading index p increase. It is also seen that the effective modulus of elasticity suddenly decreases when the material grading index increases from 0 to 1. For example, when the temperature difference is 0 K and $\alpha = 0$, the effective modulus of elasticity for $p = 0, 1, 2,$ and 3 is 2.98×10^{11}, 2.31×10^{11}, 2.09×10^{11} and 1.87×10^{11}, respectively, whereas when the temperature difference is 0 K and $\alpha = 0.2$, that is, only when the porosity ratio is increased, the effective elasticity modulus of the nanobeam becomes 2.5×10^{11}, 1.85×10^{11}, 1.63×10^{11}, and 1.41×10^{11}, respectively. Therefore, the effective elasticity modulus of the nanobeam decreases considerably with the increase of the porosity ratio.

In Fig. 4, the variation of the effective elasticity modulus according to the temperature difference is examined by considering four different porosity ratios α and three different material grading indices p. The effective
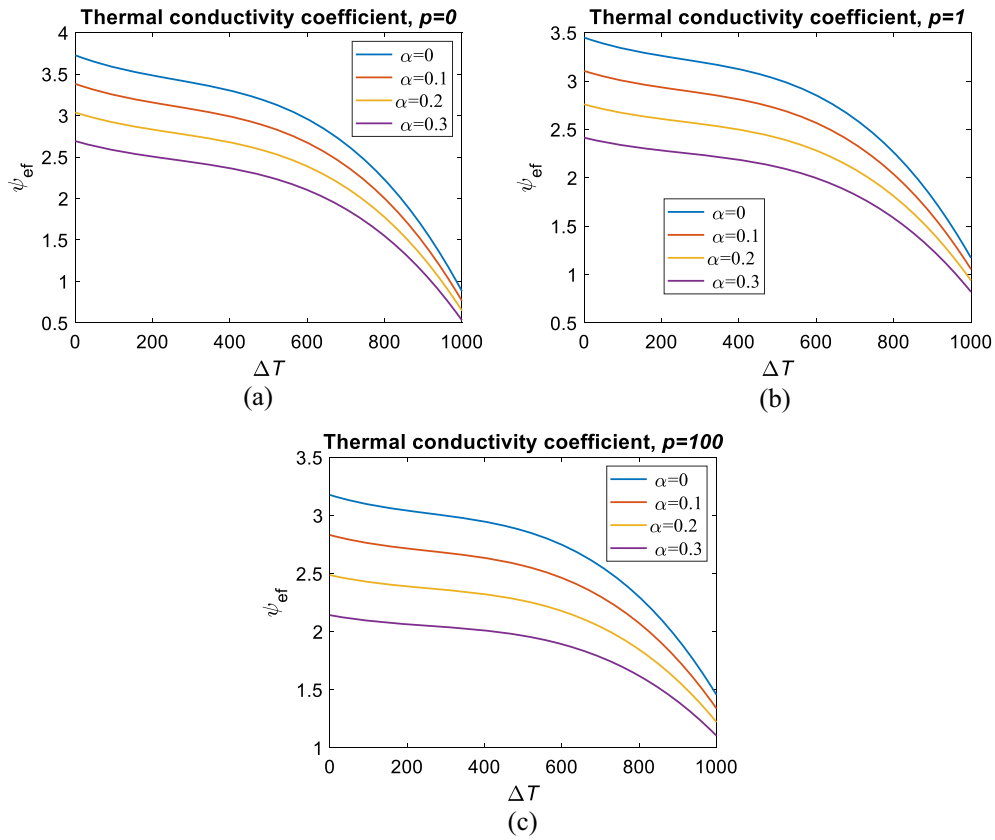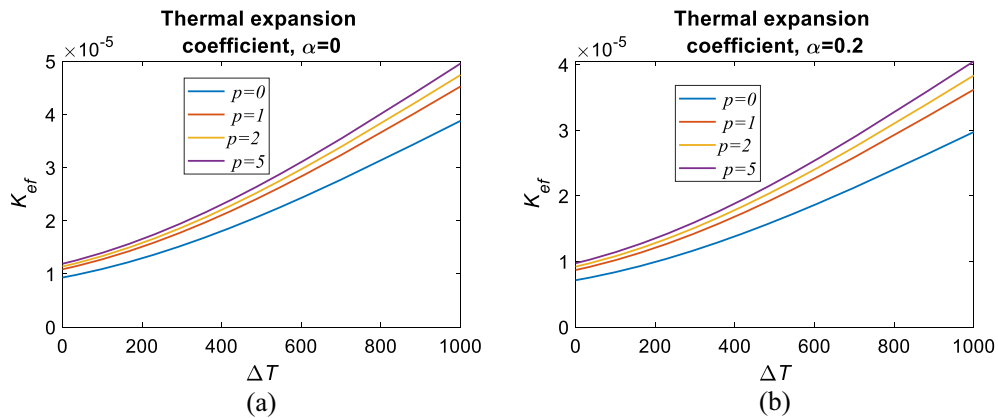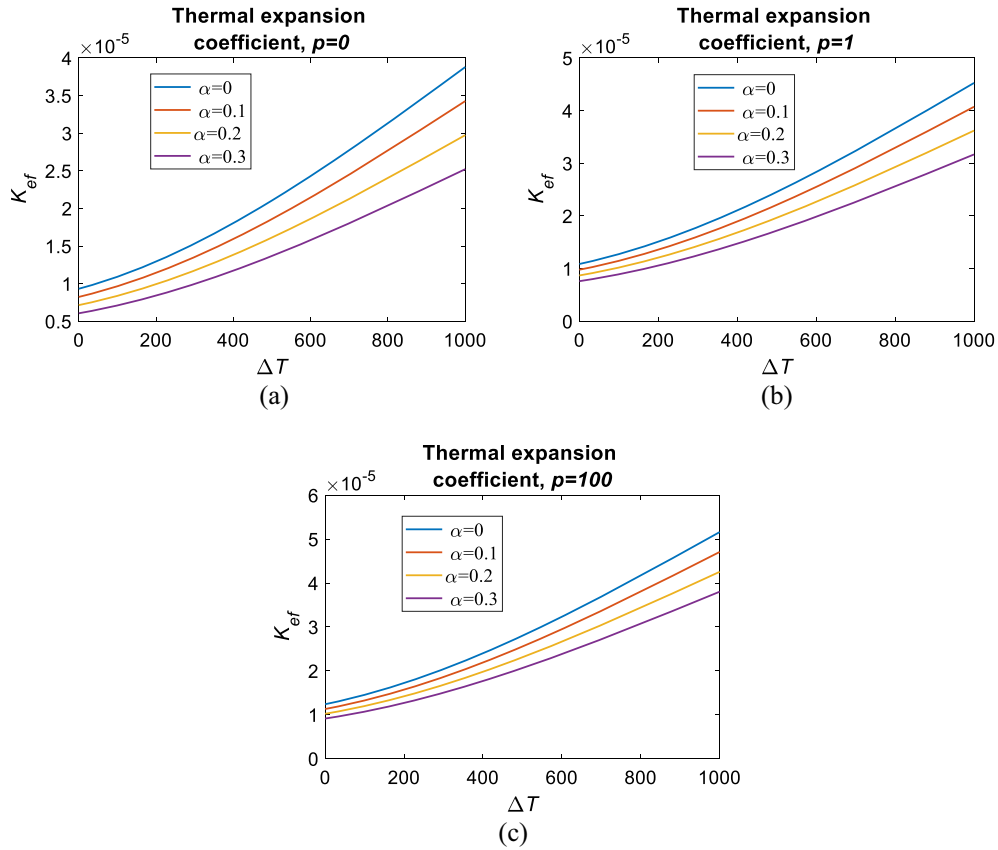
Fig. 6 Comparison of the thermal conductivity coefficient of the nanobeam depending on the four different uniform porosities ($\alpha = 0, 0.1, 0.2,$ and 0.3), material grading index p, and the ΔT in the range 0–1000 K, a) The material grading index is $p = 0$, the entire nanobeam is composed of $CoFe_2O_4$ b) At $p = 1$ the nanobeam is composed of 50% $CoFe_2O_4$ and 50% $BaTiO_3$ c) At $p = 100$, the material composition is of 99% $BaTiO_3$

Fig. 7 Comparison of the thermal expansion coefficient of the nanobeam depending on the uniform porosity (Model 1, $\alpha = 0$, and 0.2), four different material grading indices ($p = 0, 1, 2,$ and 5), and the ΔT in the range 0–1000 K, where the material grading index is $p = 0$, the entire nanobeam is composed of $CoFe_2O_4$

Fig. 8 Comparison of the thermal expansion coefficient of the nanobeam depending on the four different uniform porosities (α = 0, 0.1, 0.2, and 0.3), material grading index p, and the ΔT in the range 0–1000 K, a) At the material grading index is $p = 0$, the entire nanobeam is composed of CoFe$_2$O$_4$ b) At $p = 1$ the nanobeam is composed of 50% CoFe$_2$O$_4$ and 50% BaTiO$_3$ c) At $p = 100$, the material composition is of 99% BaTiO$_3$

Table 6 Comparisons of dimensionless frequencies of porous Model 1 beams for the ratio of porosities α, L/h, and $p = 0.6$, $e_0 a = l_m = 0$.

	λ_1			λ_2			λ_3		
α	L/h = 5	L/h = 10	L/h = 20	L/h = 5	L/h = 10	L/h = 20	L/h = 5	L/h = 10	L/h = 20
0	7.2155137	12.049875	22.681591	20.876917	29.801996	51.899693	40.071293	53.016670	83.894577
0.1	7.2244215	12.062846	22.704771	20.904593	29.827555	51.932728	40.130295	53.067688	83.947784
0.2	7.2355599	12.079213	22.734163	20.939123	29.859509	51.974220	40.203018	53.131298	84.014359
0.3	7.2498918	12.100503	22.772678	20.983395	29.900576	52.027908	40.294968	53.212807	84.100037
0.4	7.2690215	12.129365	22.825367	21.042229	29.955315	52.100128	40.415173	53.320984	84.214424
0.5	7.2958508	12.170756	22.901896	21.124170	30.031940	52.202560	40.579514	53.471527	84.374992

elasticity modulus of the nanobeam decreases with the increase of the temperature difference and the increase of the porosity ratio. When the material grading index is $p = 0$, and the porosity ratio is $\alpha = 0$, that is, when the entire material is composed of CoFe$_2$O$_4$, the effective modulus of elasticity is 2.97×10^{11}, while when the material grading index is $p = 1$, that is, when half of the beam is CoFe$_2$O$_4$ and half of BaTiO$_3$, it is 2.31×10^{11}. When almost all of the beam is BaTiO$_3$, that is, when $p = 100$, the effective elasticity modulus of nanobeam is 1.67×10^{11}. In other words, as the BaTiO$_3$ ratio increases in the nanobeam material, the effective modulus of elasticity decreases. In Fig. 5, the variation of the effective thermal conductivity coefficient of the nanobeam according to the temperature difference is investigated by considering four different material grading indices p and two different porosity ratios α. While the thermal conductivity coefficient decreases significantly with the increase of the temperature difference, with the rise of the material grading index, the thermal conductivity coefficient decreases until the temperature difference is approximately 750 K. In addition, when the porosity

Table 7 Comparisons of dimensionless frequencies of porous Model 2 beams for the ratio of porosities α, L/h, and $p = 0.6$, $e_0 a = l_m = 0$

α	λ_1			λ_2			λ_3		
	L/h = 5	L/h = 10	L/h = 20	L/h = 5	L/h = 10	L/h = 20	L/h = 5	L/h = 10	L/h = 20
0	7.2155137	12.049875	22.681591	20.876917	29.801996	51.899693	40.071293	53.016670	83.894577
0.1	7.3555059	12.310587	23.198092	21.233166	30.368097	52.916531	40.684593	53.988323	85.482582
0.2	7.5130010	12.604138	23.779535	21.636274	31.003849	54.058701	41.285873	55.079441	87.265572
0.3	7.6916122	12.937328	24.439314	22.095404	31.723431	55.351799	41.707520	56.314209	89.283234
0.4	7.8960466	13.319014	25.194885	22.622425	32.545235	56.829041	40.586620	57.723907	91.587120
0.5	8.1325617	13.760971	26.069435	23.233025	33.493687	58.534580	51.028584	59.349998	94.245659

Table 8 Comparisons of dimensionless frequencies of porous Model 3 beams for the ratio of porosities α, L/h, and $p = 0.6$, $e_0 a = l_m = 0$

α	λ_1			λ_2			λ_3		
	L/h = 5	L/h = 10	L/h = 20	L/h = 5	L/h = 10	L/h = 20	L/h = 5	L/h = 10	L/h = 20
0	7.2155137	12.049875	22.681591	20.876917	29.801996	51.899693	40.071293	53.016670	83.894577
0.1	7.2902846	12.330877	23.348129	20.972103	30.022865	52.385086	40.265617	53.378117	84.408485
0.2	7.3685880	12.589186	23.946264	21.094852	30.267471	52.891937	40.458302	53.792866	84.993866
0.3	7.4528470	12.835018	24.501225	21.249187	30.542244	53.432629	40.624065	54.273201	85.667007
0.4	7.5457988	13.077240	25.033857	21.440813	30.855469	54.022137	40.695473	54.835400	86.449562
0.5	7.6507945	13.324512	25.563431	21.677713	31.218212	54.679611	40.459930	55.501480	87.371078

Table 9 The evaluation of the porosity distribution function's impact on the porosity index $\alpha = 0.3$

$\alpha = 0.3$	$\Delta\%\lambda_1$			$\Delta\%\lambda_2$			$\Delta\%\lambda_3$		
	L/h = 5	L/h = 10	L/h = 20	L/h = 5	L/h = 10	L/h = 20	L/h = 5	L/h = 10	L/h = 20
Uniform	0.476	0.420	0.401	0.510	0.330	0.247	0.558	0.369	0.244
Symm	6.598	7.364	7.749	5.836	6.447	6.651	4.083	6.219	6.423
Asymm. Bottom	3.289	6.515	8.022	1.783	2.483	2.953	1.379	2.370	2.112

ratio increases from $\alpha = 0$ to $\alpha = 0.2$, the thermal conductivity coefficient of the nanobeam decreases. For example, when the temperature difference is 0, and the material grading index is $p = 0$, the thermal conductivity coefficient is 3.73, while when $\alpha = 0.2$, it is 3.03.

In Fig. 6, the variation of the effective thermal conductivity coefficient of the nanobeam according to the temperature difference is investigated by considering four different porosity ratios α and three different material grading indices p. In the three different graphs given, the thermal conductivity coefficient decreases significantly with the increase of the temperature difference. In addition, the increase in the porosity ratio reduces the thermal conductivity coefficient. However, as the temperature difference increases, the thermal conductivity coefficient of nanobeam decreases to zero, regardless of the porosity ratio of the material. In addition, as the material grading index p rises, the thermal conductivity coefficient decreases.

In Figs. 7 and 8, the variation of the effective thermal expansion coefficient of the nanobeam according to the temperature difference is investigated by considering four different material grading indices p and four different porosity ratios α. According to both graphs, the thermal expansion coefficient increases as the temperature difference increases. According to Fig. 7, as the material grading index increases, the thermal expansion coefficient increases, and according to Fig. 8, the porosity ratio decreases as it increases. Also, increasing the porosity ratio from $\alpha = 0$ to $\alpha = 0.2$ in Fig. 7 decreases the thermal expansion coefficient, while in Fig. 8, as the material grading index increases from $p = 0$ to $p = 100$, the thermal expansion coefficient decreases.

4.3 Free vibration behavior depending on slenderness ratio and porosity index

Detailed analyses were made for the variation of the dimensionless frequencies of the nanobeam according to the porosity distribution functions, and the results are presented in Tables 6, 7, 8. Table 6 shows the variation
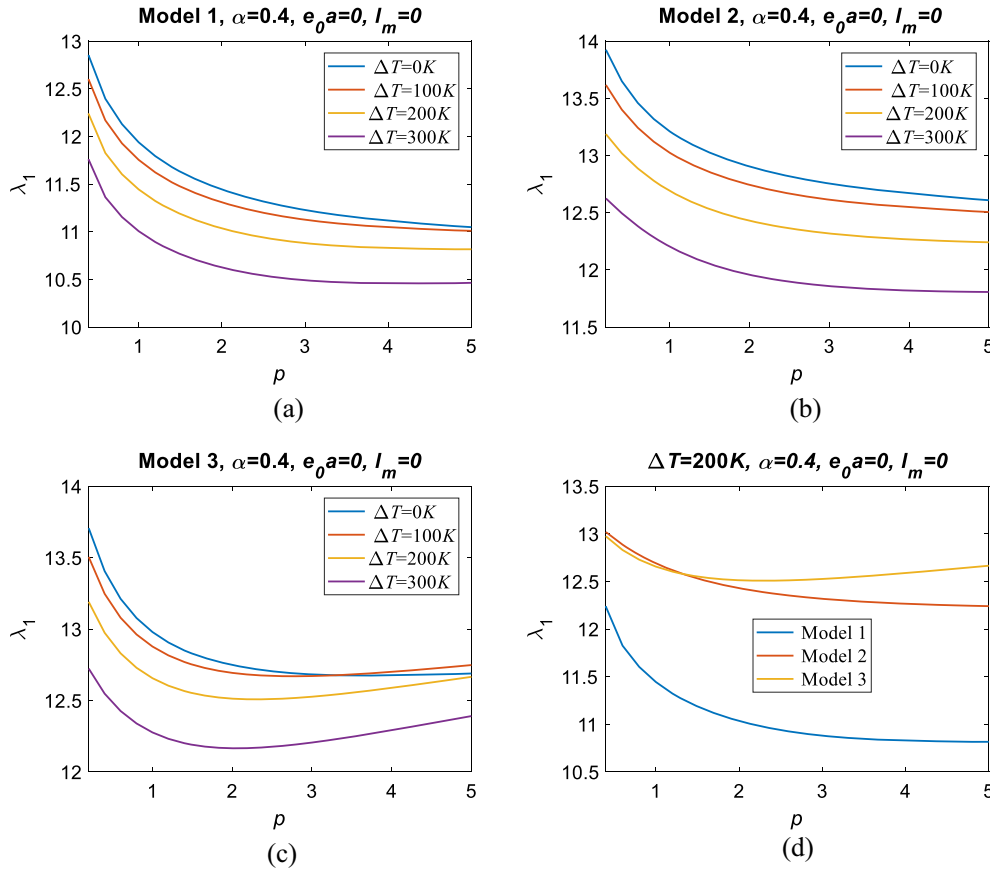
Fig. 9 Variation of the dimensionless frequencies λ_1, λ_2 and λ_3 depending on temperature difference and material grading index p; for the uniform porosity distribution model (Model 1): for $\alpha = 0.4$, nonlocal parameter $e_0 a = 0$ and material size factor $l_m = 0$. **a** For uniform porosity model (Model 1) **b** For symmetric porosity model (Model 2) **c** For asymmetric ascending downward porosity model (Model 3) **d** Comparison for three different Models

of the first three dimensionless natural frequencies λ_1, λ_2, and λ_3 for aspect ratios L/h = 5, 10, and 20 and the porosity ratios $\alpha = 0$, 0.1, 0.2, 0.3, 0.4, and 0.5 for uniform porosity distribution function given in Model 1. Dimensionless frequencies are shown in Table 7 for the symmetric porosity distribution function given in Model 2, and in Table 8 for the asymmetric ascending downward porosity distribution function given in Model 3. In Table 9, the differences between $\alpha = 0.3$ and $\alpha = 0$ porosity are presented comparatively according to three different porosity distribution models.

According to the formula: $\Delta\%\lambda_i = \frac{\lambda_{i,\alpha=0.3}}{\lambda_{i,\alpha=0}}100 - 100$, the relative variation of the first three vibration frequencies of porous FGM beams is calculated. The results are shown in Table 9 for all taken into consideration porosity models at $\alpha = 0.3$. With a uniform porosity distribution, the relative increase in frequencies is approximately 0.24–0.56%; however, for an asymmetric bottom distribution, it is observed to be between 1.38 and 8.02%. But for the symmetric distribution, a significant increase of 4–7.33% is noted.

4.4 Case study: free vibration behavior depending on nonlocal parameters and porosity index

In this chapter, the free vibration behaviors of the FG nanobeam, various porosity coefficient α and porosity distribution functions (Model 1, Model 2, and Model 3), nonlocal parameter $e_0 a$, material gradient index p, temperature difference ΔT, the material size factor l_m, aspect ratio L/h, electric potential coefficients v, and magnetic potential coefficients ε are taken into account in detail. In addition, the buckling behavior of the temperature-dependent nanobeam was investigated in detail.

When the temperature difference is at 0 K and $p = 0.4$, the dimensionless first frequency λ_1 decreases from 12.84 to 11.04 at $p = 5$ (17% $CoFe_2O_4$, 83% $BaTiO_3$). If the temperature rise difference is at $\Delta T = 100$ K, the
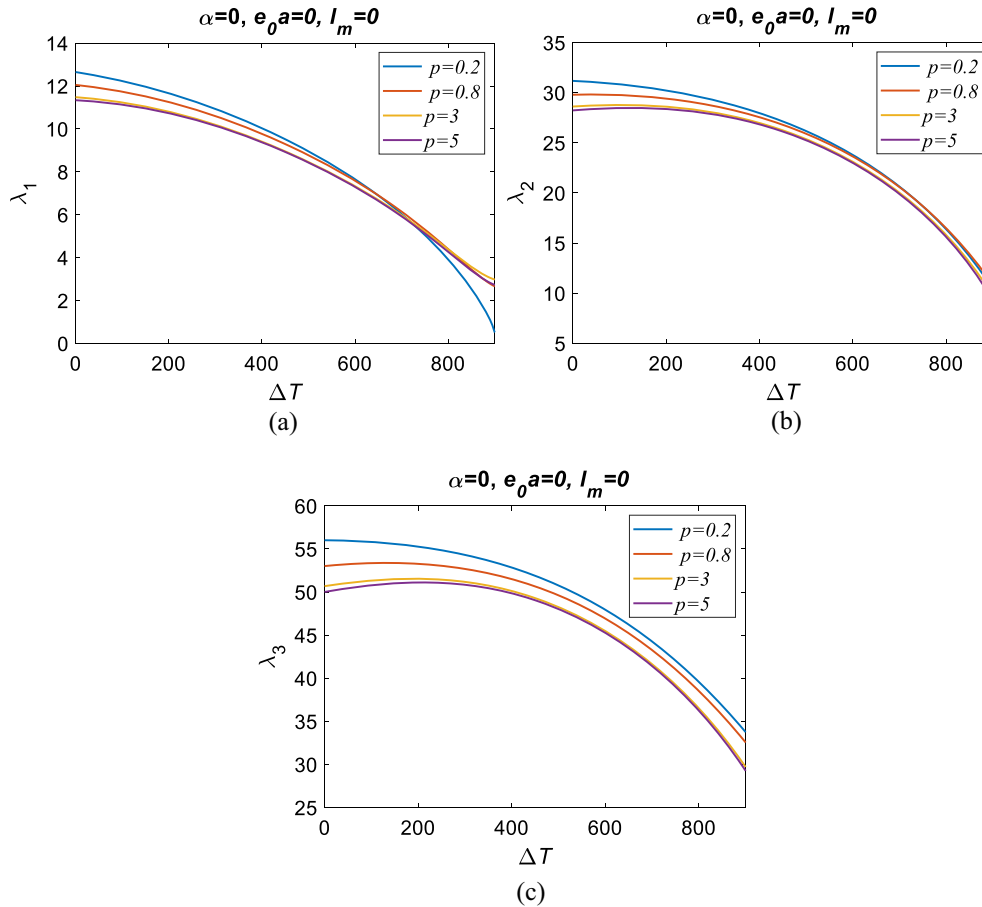
Fig. 10 Variation of the dimensionless frequencies λ_1, λ_2 and λ_3 depending on the temperature difference ΔT and four material grading indices $p = 0.2\ 0.8\ 3\ 5$ for $\alpha = 0$, nonlocal parameter $e_0 a = 0$ and material size factor $l_m = 0$

first dimensionless natural frequency decreases from 12.6 at $p = 0.4$ to 11 at $p = 5$. Comparing the situation at $p = 0.4$, the $\Delta T = 100$ K temperature difference reduces the natural frequency by 1.87%. If the temperature rise difference is $\Delta T = 200$ K, the first dimensionless natural frequency decreases from 12.23 at $p = 0.4$ to 10.81 at $p = 5$. If the temperature difference is $\Delta T = 300$ K, the first dimensionless frequency is 11.75 at $p = 0.4$ and 10.46 at $p = 5$. Comparing the situation at $p = 0.4$, the $\Delta T = 200$ K temperature difference reduces the natural frequency by 4.75%. As can be seen, the decrease in temperature difference at 100 K is 1.87%, while the reduction in temperature difference at 200 K is 4.75%. The decrease rate is nonlinear because the change of material properties depending on temperature is nonlinear, as given in Eq. (5). For Model 1 and Model 2, the dimensionless frequencies reduce as the material grading index rises. In contrast, for Model 3, the frequency decreases until the material grading index becomes $p = 2$ and rises after this value (Fig. 9).

The material grading index p has an essential place in the frequency behavior of the nanobeam because the material grading index describes the material composition of the nanobeam. The formula calculates the volume fractions of $CoFe_2O_4$ and $BaTiO_3$ concerning p in Eq. 1. Accordingly, at $p = 0$, the entire nanobeam is composed of $CoFe_2O_4$. At $p = \infty$, the entire nanobeam material consists of $BaTiO_3$. In the case of $p < 2$, natural frequencies are higher because the $CoFe_2O_4$ in the nanobeam is high, and the elasticity of $CoFe_2O_4$ is high. If the $p > 2$, the decrease in frequencies reduces with the increase of $BaTiO_3$ in the nanobeam, and at high p values, for example ($p = 4.5$), the reduction in frequencies goes toward the limit. This is because almost all of the beam material is made up of $BaTiO_3$. In other words, at high p values, the beam material becomes homogeneous. For example, at $p = 5$, the $CoFe_2O_4$ ratio in the beam material is 17%, and the $BaTiO_3$ ratio is 83%.
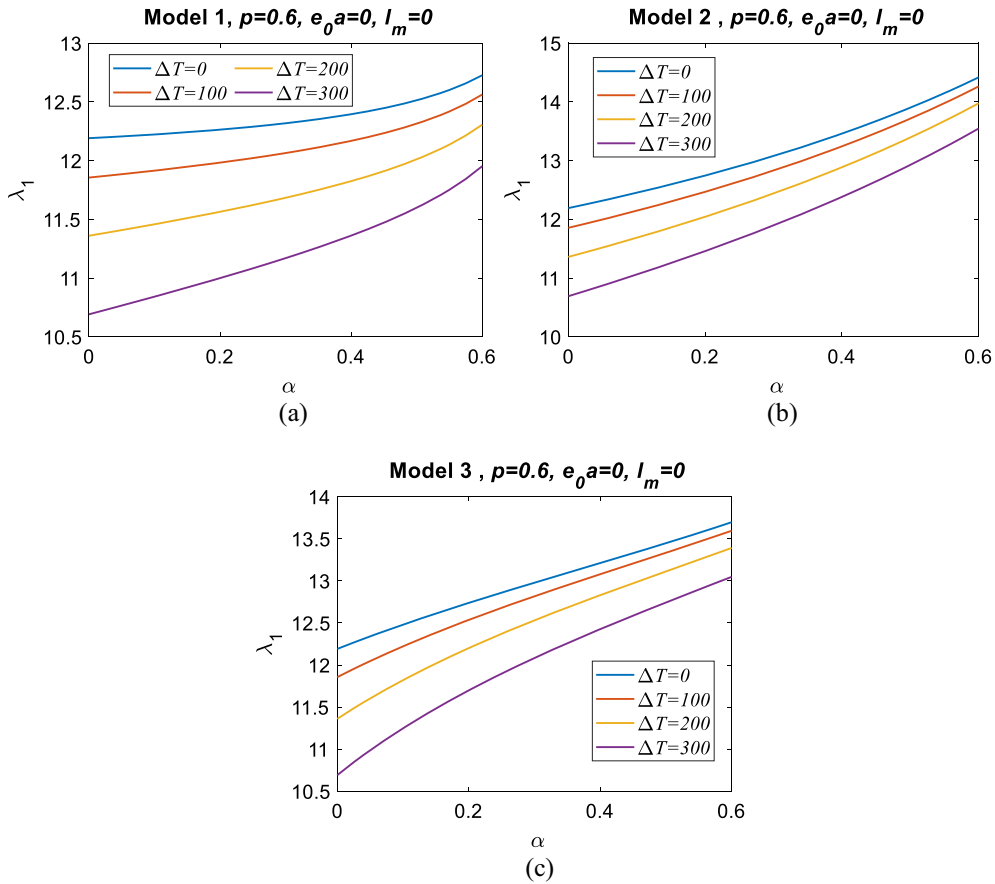
Fig. 11 Variation of the dimensionless frequencies λ_1 of different porosity models depending on the material grading index $p = 0.6$, nonlocal parameter $e_0a = 0$, material size factor $l_m = 0$, and temperature difference $\Delta T = 0$, 100, 200 and 300K

In Fig. 10, the dimensionless natural frequencies are examined according to the temperature difference in four different cases with the material grading index $p = (0.2\ 0.8\ 3\ 5)$. When the material grading index is 0.2, 0.8, 3, and 5, 83.3%, 55.5%, 25%, and 16% of the beam material is composed of $CoFe_2O_4$, while the remainder is composed of $BaTiO_3$. As the material grading index rises, the first three natural frequencies decrease. For the material composition (83.3% $CoFe_2O_4$, 16.6% $BaTiO_3$) at material grading index $p = 0.2$, when the temperature difference is 0 K, the first natural frequency is 12.65, and when the temperature difference is 900 K, it becomes buckling.

Dimensionless first natural frequency variation of uniform, symmetric, and bottom models for porosity ratio $\alpha = 0$–0.6 is given according to $\Delta T = 0$, 100, 200, and 300 K temperature differences and material grading coefficient $p = 0.6$. As the temperature difference increased, the first and second natural frequencies generally decreased, while the third natural frequency showed variable characteristics. But, as the porosity ratio increases, all natural frequencies increase. The first dimensionless natural frequency is 12.2 for all models when the temperature difference is 0 K and $\alpha = 0$, while it is 12.73 for Model 1, 14.41 for Model 2, and 13.7 for Model 3 when the temperature difference is 0 K and $\alpha = 0.6$. That is, an increase in the porosity ratio from 0 to 0.6 increases the dimensionless first natural frequency for Model 1, Model 2, and Model 3 by 4.34%, 18.11%, and 12.3%, respectively. When the other temperature differences are examined, the dimensionless first natural frequency increase is almost the same. As the porosity ratio increases, the temperature-dependent dimensionless frequency variation graphs converge in all models. This is because thermal conductivity decreases due to high porosity, and the effect of temperature occurs. Besides the presence of porosity, it can be seen from the figures that the distribution function of porosity affects the natural frequency of the nanobeam. For example, when the uniform porosity distribution in Fig. 11a, the symmetrical porosity distribution in Fig. 11b, and the near-subsurface porosity distribution in Fig. 11c are compared with each other, a rapid increase in symmetrical
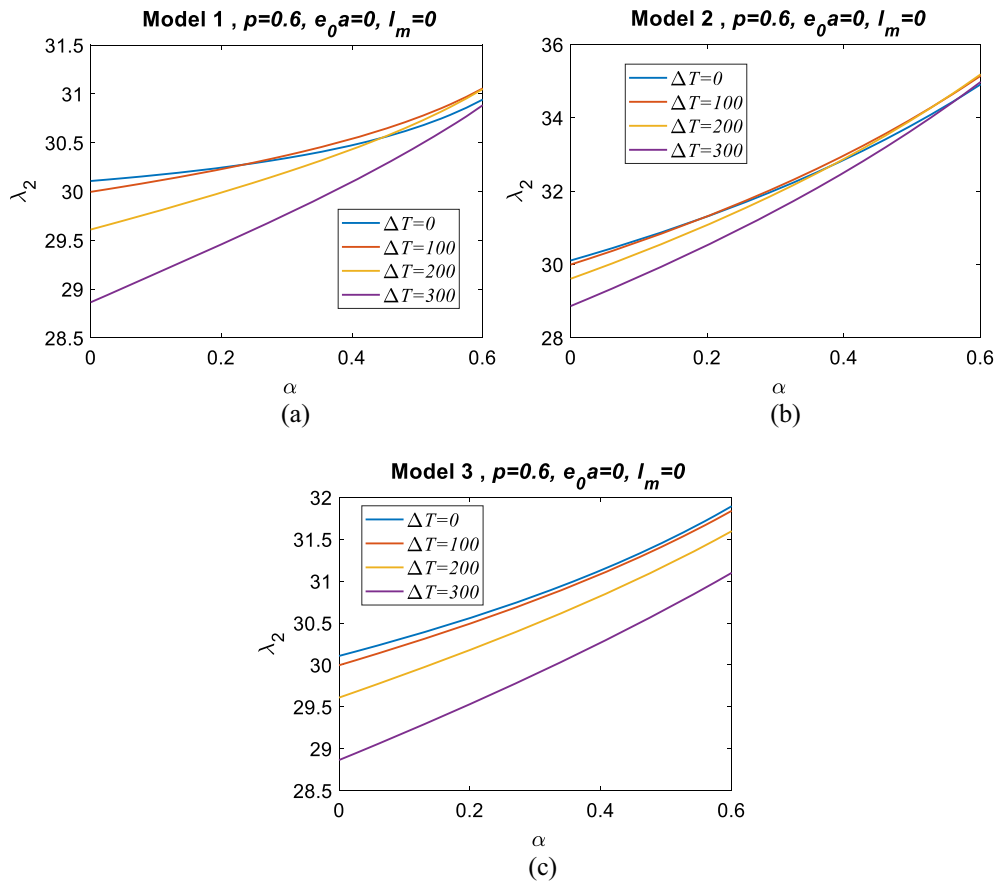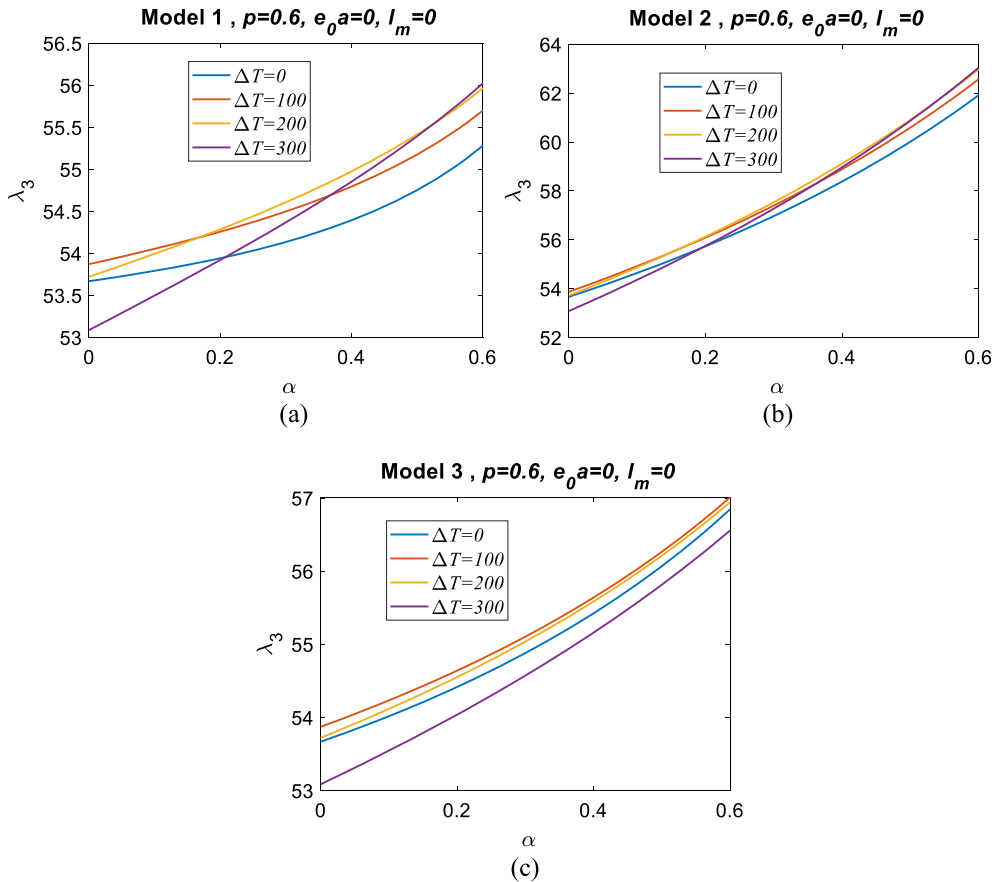
Fig. 12 Variation of the dimensionless frequencies λ_2 of different porosity models depending on the material grading index $p = 0.6$, nonlocal parameter $e_0a = 0$, material size factor $l_m = 0$, and temperature difference $\Delta T = 0$, 100, 200 and 300K

porosity, a slightly slower rise in uniform porosity than symmetrical porosity, and the slowest increase in the lower surface porosity model are observed (Fig. 12).

The second dimensionless natural frequency is 30.1 for all Models when $\alpha = 0$ and $\Delta T = 0$, and 30.9, 34.9 and 31.9 for Model 1, Model 2, and Model 3 when $\alpha = 0.6$ and $\Delta T = 0$, respectively. That is, the increase in the porosity ratio increases by 2.6%, 15.9%, and 5.98%, respectively. If the dimensionless second natural frequency is $\Delta T = 100$, it increases by 3.5%, 17.16%, and 6.13% for Model 1, Model 2, and Model 3, with the increase in porosity ratio from 0 to 0.6, respectively. Similarly, when $\Delta T = 200$, the porosity ratio increases from 0 to 0.6, it increases by 4.89%, 18.8%, and 6.75% for Model 1, Model 2, and Model 3, respectively. In the case of $\Delta T = 300$ K, it increases by 7.22%, 21.5%, and 7.98% for Model 1, Model 2, and Model 3, respectively, with an increase in the porosity ratio from 0 to 0.6. In addition, the increase in the porosity ratio increases the natural frequency, while the rise in the temperature difference increases the natural frequency even more.

Fig. 13 Variation of the dimensionless frequencies λ_3 of different porosity models depending on the material grading index $p = 0.6$, nonlocal parameter $e_0a = 0$, material size factor $l_m = 0$, and temperature difference $\Delta T = 0$, 100, 200 and 300K

According to Fig. 13, the dimensionless third natural frequency was 53.66 when $\alpha = 0$ and $\Delta T = 0$, while the porosity value increased to 55.2 for Model 1, 61.9 for Model 2, and 56.85 for Model 3 when the porosity value was 0.6. With the increase in the porosity ratio, the value of the dimensionless third natural frequency increased by 2.87% for Model 1, 15.35% for Model 2, and 5.94% for Model 3.

In Fig. 14, the variation of the first dimensionless natural frequency is given according to the temperature difference in the case of material grading coefficient $p = 0.6$ and three different porosity ratios. According to the graph, as the temperature difference increases, the value of the dimensionless natural frequency decreases until the temperature difference is 950 K. When this temperature difference is reached, the natural frequency values increase considerably. In addition, the natural frequency reduces with the rise of the temperature difference, while the natural frequency rises as the porosity ratio increases. If $\alpha = 0$, the natural frequency gets its lowest value at 930 K. If $\alpha = 0.2$, 0.4, and 0.6, the lowest value for Model 1 is at 950 K, 980 K, and 1050 K, respectively, and the lowest value for Model 2, respectively. It gets at 950 K, 975 K, and 1010 K. Regardless of the porosity value for Model 1, if the temperature difference is 1073 K, the dimensionless natural frequency value will be the same, while for Model 2, this temperature difference will be 1090 K.
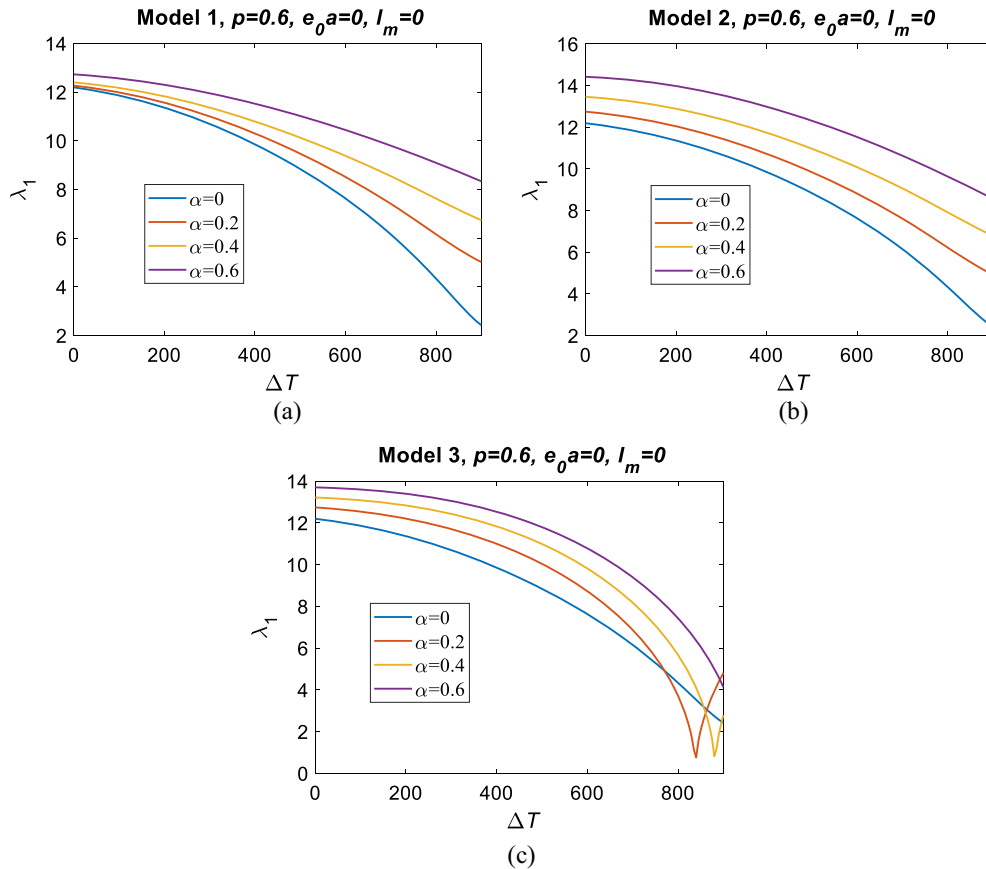
Fig. 14 Variation of the dimensionless frequency λ_1 of different temperature differences ΔT depending on the material grading index $p = 0.6$, nonlocal parameter $e_0 a = 0$, material size factor $l_m = 0$, and different porosity models

In Fig. 15, the variation of the first dimensionless frequency is given according to the porosity ratios α, temperature difference $\Delta T = 0$ K, and material grading index $p = 0.8$, 1, 2, and 5 for three different material models. In Fig. 15b and c, the first dimensionless frequency rises as the porosity increases. But, in Fig. 15a, the frequency decreases as the porosity ratio increases. When Fig. 15 is examined, if the material grading index is $p = 5$, when $\alpha = 0$, the dimensionless first frequency is 11.34 for all Models, and if $\alpha = 0.6$, it is 10.98, 13.58 and 13.29 for Model 1, Model 2, and Model 3, respectively. In other words, as the porosity rise, the dimensionless frequency in Model 1 decrease by 3.17%, while it rise by 19.75% and 17.19% for Model 2 and Model 3, respectively. In Fig. 15d, three models are given according to the change in porosity. Accordingly, as the porosity ratio increases, the first dimensionless frequency decreases for Model 1, while it increases considerably for Model 2 and Model 3.

In Fig. 16, the variation of the first dimensionless three frequencies is examined in the case of material grading coefficient $p = 0$–5, temperature difference $\Delta T = 0$ K and four different beam aspect ratios L/$h =$ 10, L/$h = 20$, L/$h = 30$, and L/$h = 50$. It is understood from the graphs that as the aspect ratio increases, all dimensionless frequencies increase.
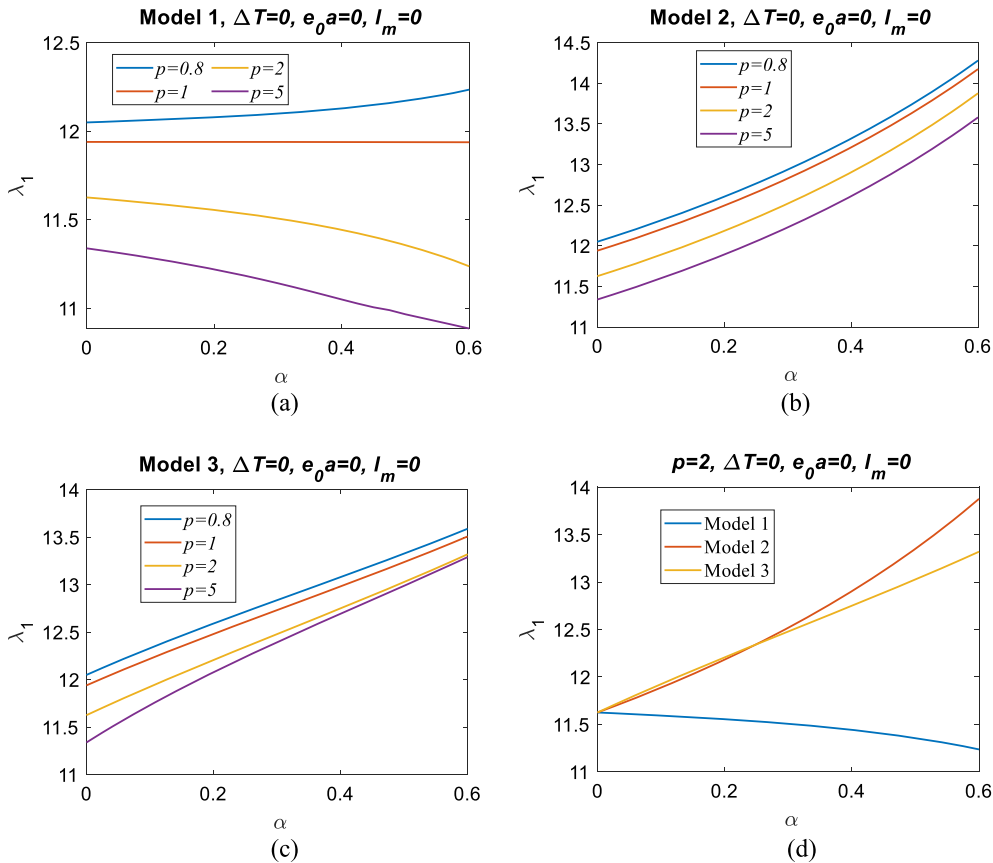
Fig. 15 Variation of the dimensionless frequencies λ_1 of porosity α depending on material grading index $p = 0.8$, 1, 2, 5, the material size factor $l_m = 0$ and nonlocal parameter $e_0a = 0$

Figure 17 examines the effect of four different beam aspect ratios on the first three dimensionless frequencies when $\Delta T = 0$–800. According to the graphs, while the dimensionless frequency increases as the aspect ratio rises, the frequency decreases considerably as the temperature difference increases. In Fig. 17a, if $\Delta T = 0$ and the beam aspect ratio is $L/h = 10$, $L/h = 20$, $L/h = 30$, and $L/h = 50$, the dimensionless first frequency is 12.19, 22.92, 33.95, and 56.22, respectively. With the rise of the temperature difference, if the beam aspect ratio is $L/h = 50$, the dimensionless frequency decreases to 0 at $\Delta T = 715$ K and becomes buckling. If the beam aspect ratio is $L/h = 30$ and $L/h = 20$, buckling occurs at $\Delta T = 730$ K and $\Delta T = 755$ K, respectively. If the beam aspect ratio is $L/h = 10$, the dimensionless frequency is reduced to 2.89 at a temperature difference of $\Delta T = 800$ K. In addition, in the case where the temperature difference is $\Delta T = 706$ K, the dimensionless frequency value of the whole beam aspect ratio is the same.

To demonstrate how the material size factor $l_m = 0$, 1, 2, and 4 nm^2 affects the strain gradient elasticity, Fig. 18 shows the effect of temperature change and material size factor on the dimensionless fundamental frequency. Generally, as can be seen from the figure, the increase in the material size factor increases the fundamental frequency depending on the value of the size factor. This is because the material size factor creates a stiffness that enhance the effect in the nanobeam. But the dimensionless frequency decreases as the temperature difference increases. For example, when the temperature difference is $\Delta T = 0$, the dimensionless frequencies for $l_m = 0$, 1, 2, and 4 nm^2 are 12.19, 12.62, 13, and 13.72, respectively, while in the case of $\Delta T = 900$, they are 2.41, 4.49, 5.74, and 7.47, respectively. In other words, as the temperature difference increases, the rate of decrease in frequencies becomes 80%, 64.42%, 55.84%, and 45.55%. In this case, the maximum reduction rate occurs when $l_m = 0$.
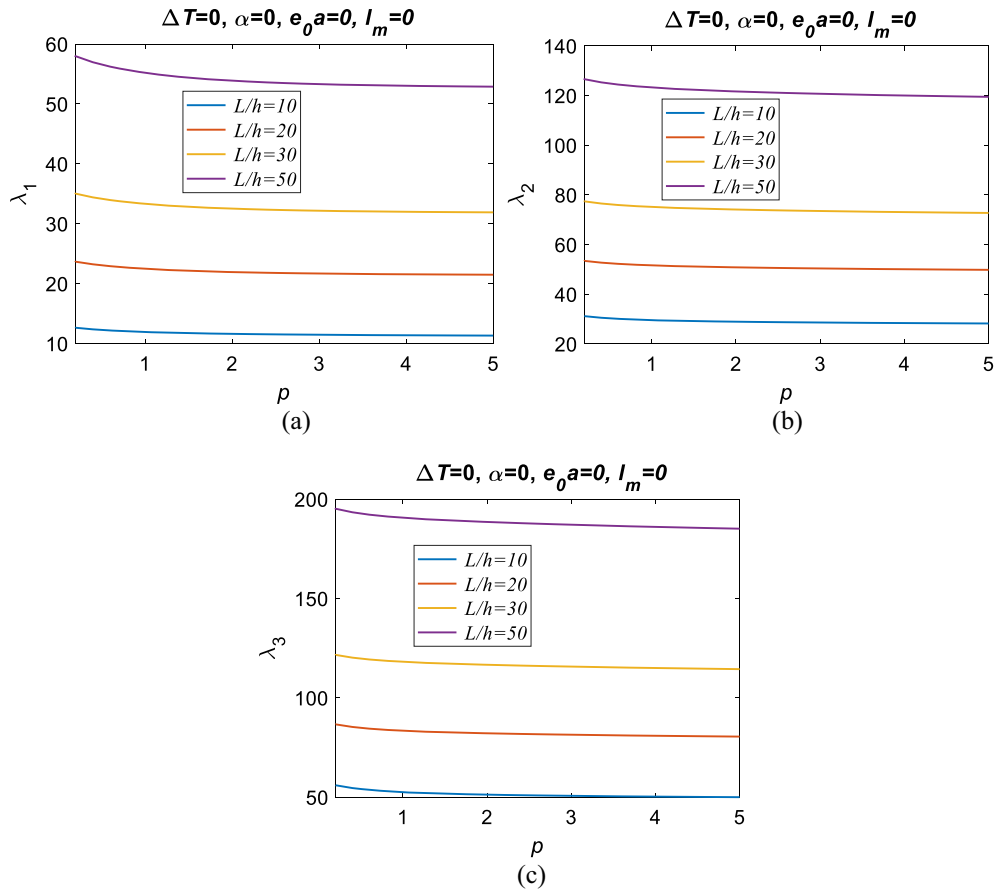
Fig. 16 Variation of the dimensionless frequencies λ_1 of material grading index $p = 0$, depending on temperature difference $\Delta T = 0$, porosity$\alpha = 0$, the material size factor $l_m = 0$ and nonlocal parameter $e_0 a = 0$

In Fig. 19, the variation of the first three dimensionless frequencies is given if the material grading index is $p = 0.6$, temperature difference $\Delta T = 0$, material porosity $\alpha = 0$–0.6, and four different dimensionless magnetic potential coefficients $\varepsilon = 0$, 0.0001, 0.0002, 0.0003. According to the graph, as the material porosity and magnetic potential coefficient increase, the dimensionless frequency increases. However, the increase in the magnetic potential coefficient was more effective on the rise of the dimensionless frequency than the increase in the porosity. For example, the value of the dimensionless first frequency is 12.19 when the dimensionless magnetic potential coefficient is $\varepsilon = 0$, and the porosity ratio is $\alpha = 0$ and 12.72 when $\alpha = 0.6$. In other words, with the increase in porosity, the dimensionless first frequency increased by 4.35%. However, if $\alpha = 0$, $\varepsilon = 0.0003$, the dimensionless first frequency increased by 70.3% to 20.76. In addition, if $\alpha = 0.6$ and $\varepsilon = 0.0003$, the dimensionless first frequency took the value of 22.9 and increased by 10.3% with the increase in porosity. As can be understood from these data, the effect of porosity became more pronounced as the dimensionless magnetic coefficient increased.

In Fig. 20, the variation of the first three dimensionless frequencies is given if the material grading index is $p = 0.6$, temperature difference $\Delta T = 0$, material porosity $\alpha = 0$–0.6, and four different dimensionless electric potential coefficients $v = 0$, 0.001, 0.002, 0.003. According to the graphs, the dimensionless frequencies increase with the increase of both the porosity ratio and the dimensionless electric potential coefficient.
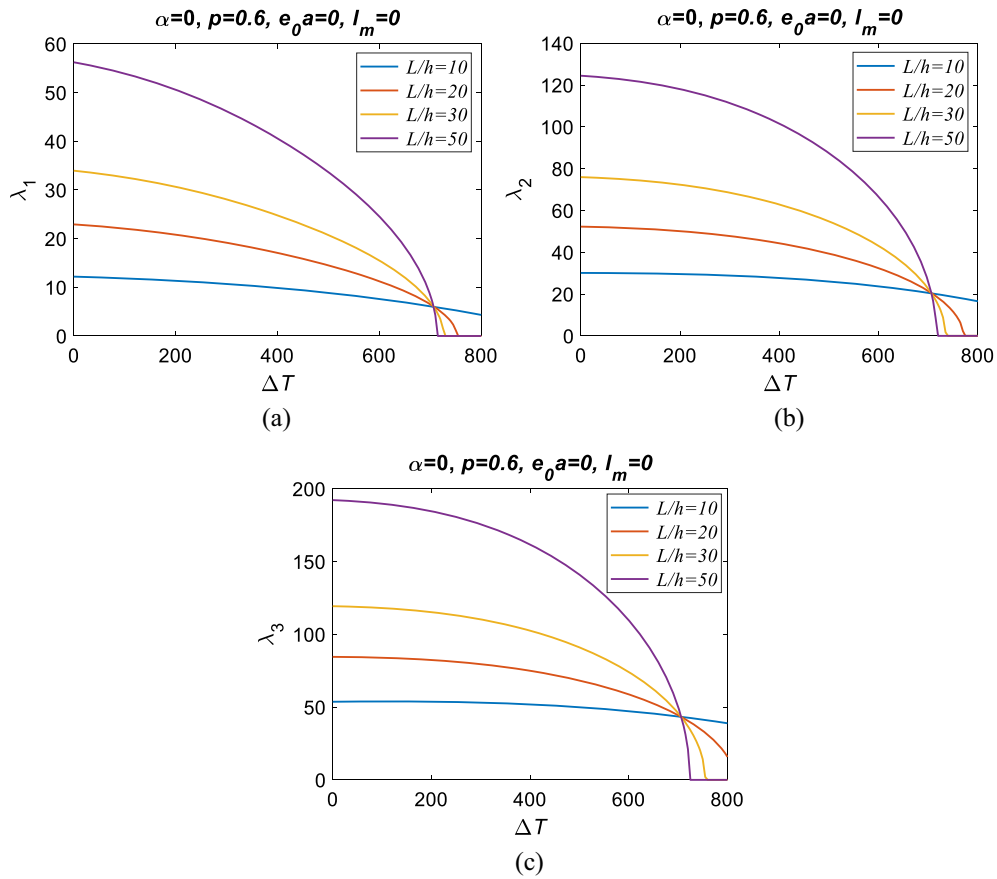
Fig. 17 Variation of the dimensionless frequencies of material grading index $p = 0$, depending on temperature difference $\Delta T = 0$, porosity $\alpha = 0$, the material size factor $l_m = 0$, and nonlocal parameter $e_0 a = 0$
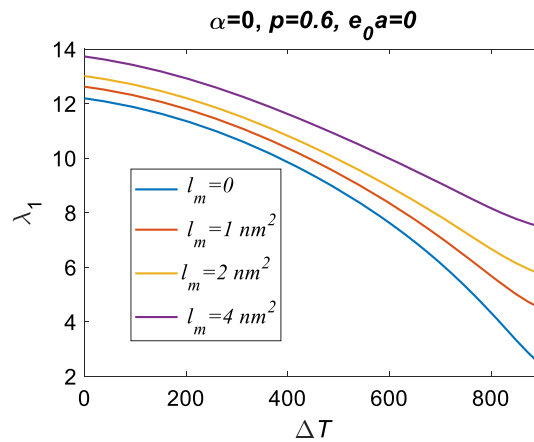

Fig. 18 Variation of the dimensionless frequencies λ_1 of different temperature differences ΔT depending on the material grading index $p = 0.6$, nonlocal parameter $e_0 a = 0$, porosity $\alpha = 0$, and different material size factors l_m
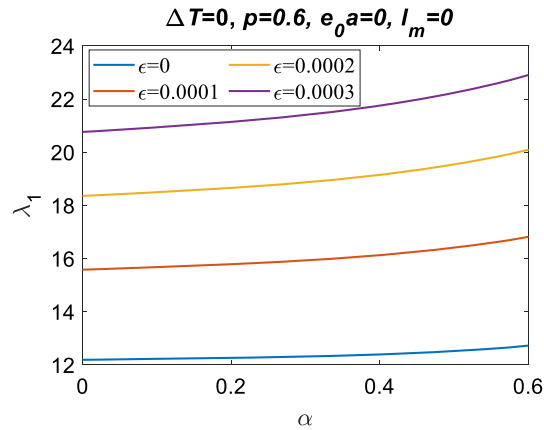
Fig. 19 Variation of the dimensionless frequencies λ_1 of porosity α depending on the material size factor $l_m = 0$, temperature difference $\Delta T = 0$, the material grading index $p = 0.6$, nonlocal parameter $e_0 a = 0$, and different dimensionless magnetic potentials
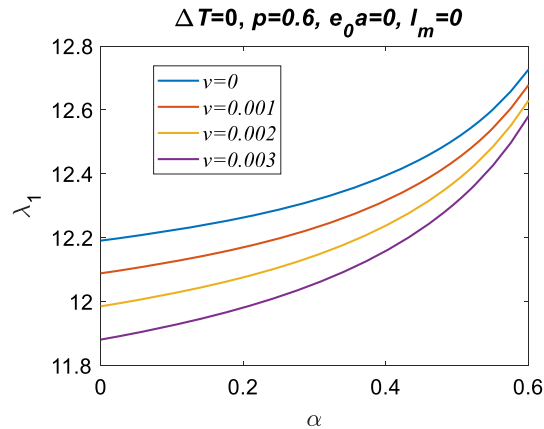

Fig. 20 Variation of the dimensionless frequencies λ_1 of porosity α depending on the material size factor $l_m = 0$, temperature difference $\Delta T = 0$, the material grading index $p = 0.6$, nonlocal parameter $e_0 a = 0$, and different dimensionless electric potentials

In Fig. 21, the variation of the first three dimensionless frequencies for the temperature difference $\Delta T = 0$, porosity ratio $\alpha = 0$ is investigated in the case of four different dimensionless magnetic potential coefficients $\varepsilon = 0, 0.0001, 0.0002, 0.0003$, and material grading coefficient $p = 0$–6. As the material grading coefficient increases, the dimensionless frequencies decrease, while as the dimensionless magnetic field coefficient increases, the frequencies increase. When the effect of magnetic potential is examined, when the material grading coefficient is $p = 2$, and the magnetic potential coefficient is $\varepsilon = 0$ and $\varepsilon = 0.0003$, the dimensionless first natural frequency is 11.63 and 16.87, respectively. In other words, the increase in frequency is approximately 45%. In the same cases, the increase rate of the second dimensionless frequency is 27%, while the increase rate of the third dimensionless frequency is 20%.

In Fig. 22, the variation of the first three dimensionless frequencies for the temperature difference $\Delta T = 0$, porosity ratio $\alpha = 0$ is examined when four different dimensionless electric potential coefficients $v = 0$, $0.001, 0.002, 0.003$ and the material grading index varies between $p = 0$–6. As the material grading index increases, the dimensionless frequencies decrease, and the frequencies decrease as the dimensionless electric field coefficient increases. For example, when $p = 0.2$, the dimensionless first frequency is 12.65, 12.61, 12.56, and 12.51 for $v = 0, 0.001, 0.002$, and 0.003, respectively, and 11.34, 11.09, 10.8, and 10.59 when $p = 5$. In this case, it is understood that as the dimensionless electric field coefficient increases, the rate of decrease in frequencies also increases.

Everything is the same in the given graph compared to the previous one; only the material grading index is analyzed according to $p = 0.5$ instead of $p = 2$. When both figures are examined, it is seen that the frequency
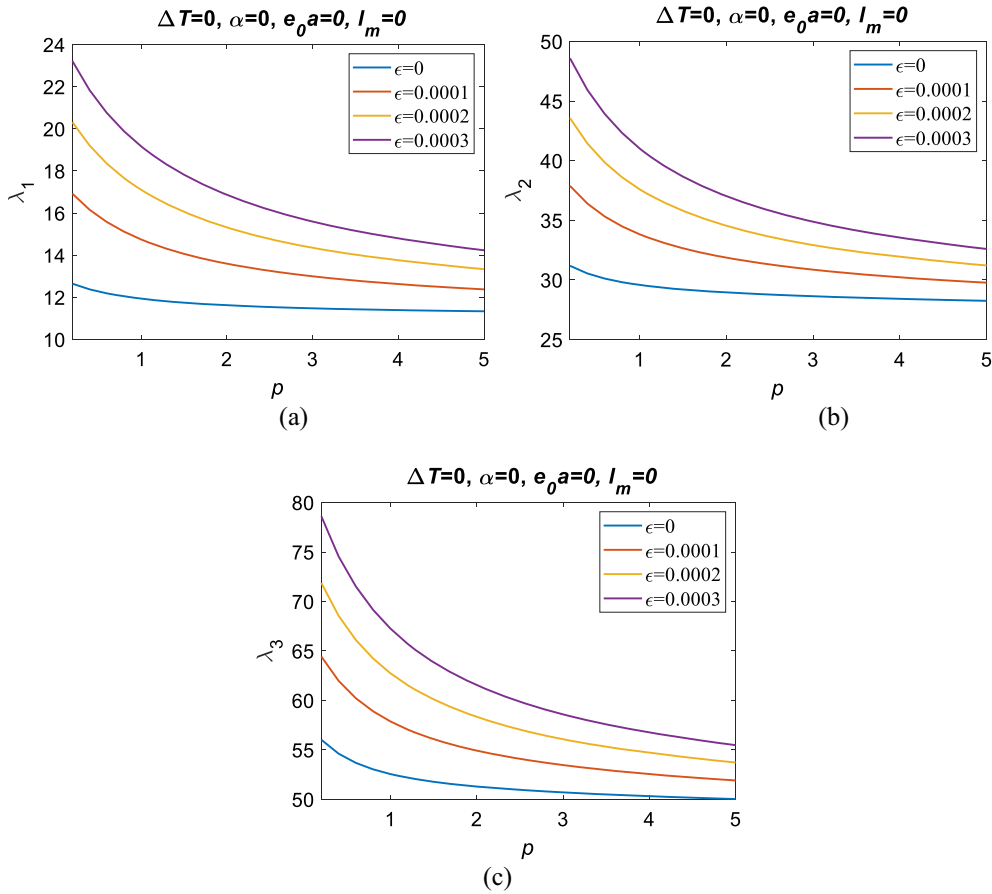
Fig. 21 Variation of the dimensionless frequencies of material grading index p, depending on temperature difference $\Delta T = 0$, porosity $\alpha = 0$, nonlocal parameter $e_0 a = 0$, and the material size factor $l_m = 0$, and different dimensionless magnetic potentials

value increased from approximately 11.3 to 12.1 while $\Delta T = 0$ K with the decrease of the material grading index. In addition, when $\Delta T = 770$ K and $p = 2$, the frequency drops to 0, and buckling occurs.

In Fig. 23, according to the material grading index, which varies between $p = 0$–6 for the porosity ratio $\alpha = 0$, temperature difference $\Delta T = 0$, nonlocal parameter $e_0 a = 0$, and material size factor $l_m = 0, 1, 2$, and 4, the variation of the dimensionless first frequency is given. Increasing the material grading index decreases the frequencies, while reducing the material size factor raises the frequencies. According to the graph, with the increase of the material grading index p, the dimensionless frequency decrease from 12.65 to 11.33 when $l_m = 0$, from 13.11 to 11.71 when $l_m = 1$, from 13.52 to 12.05 when $l_m = 2$, and from 14.3 to 12.67 when $l_m = 4$. In this case, the maximum reduction rate occurs when $l_m = 4$ with 11.39%. The decrease rate in other material size factor values is approximately 10.6%.

Figure 24 shows the first dimensionless frequency variations depending on porosity distribution, four different nonlocal parameters, and the composition of the materials for a constant porosity index $\alpha = 0.2$. According to the graphs, as the material grading index increases, the dimensionless frequency decreases for all three models. However, the dimensionless frequency decreases rapidly when the material grading index is between 0 and 1. The effect of the nonlocal parameter is noticeable as a decrease in the frequency. In other words, as the nonlocal parameter increases, the frequency values decrease partially. In the case of nonlocal parameter $e_0 a = 0, 1, 2$ in the uniform porosity (Model 1) and symmetric porosity (Model 2) models, the frequency values are almost the same, while when $e_0 a = 4$, the frequency values decrease in Model 1 and Model 2. In Fig. 24d, three different porosity models are examined to determine if $e_0 a = 2$. So, while the highest decrease in frequency was observed in Model 1, the least decrease occurred in Model 2.
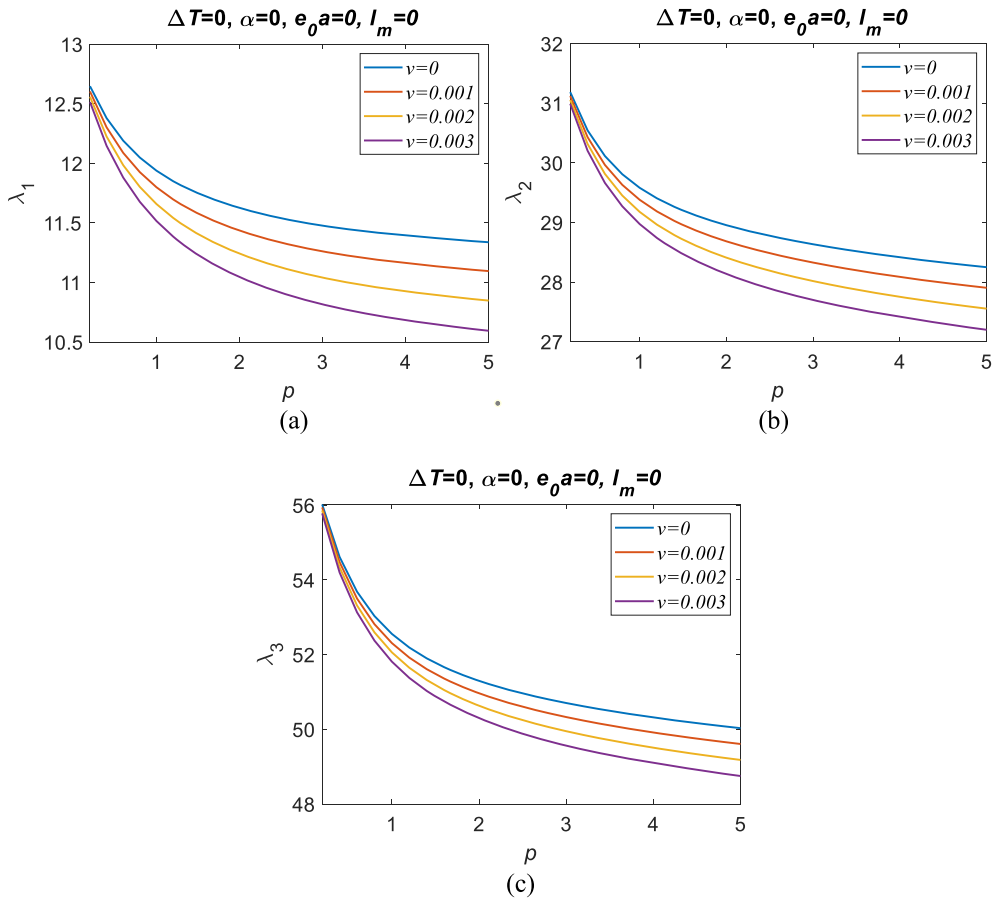
Fig. 22 Variation of the dimensionless frequencies of material grading index p, depending on temperature difference $\Delta T = 0$, porosity $\alpha = 0$, nonlocal parameter $e_0 a = 0$, and the material size factor $l_m = 0$, and different dimensionless electric potentials
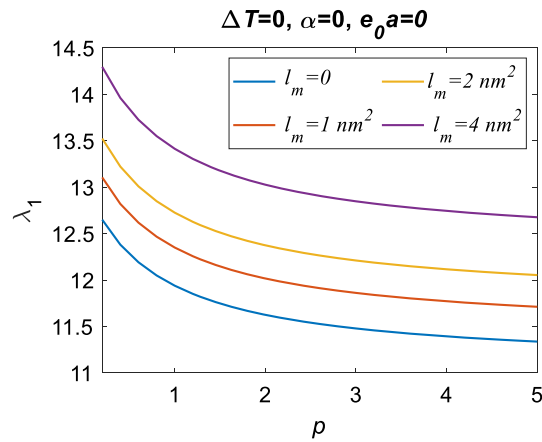

Fig. 23 Variation of the dimensionless frequency λ_1 of material grading index p depending on temperature difference $\Delta T = 0$, porosity $\alpha = 0$, nonlocal parameter $e_0 a = 0$, and the material size factor $l_m = 0$, and different nonlocal
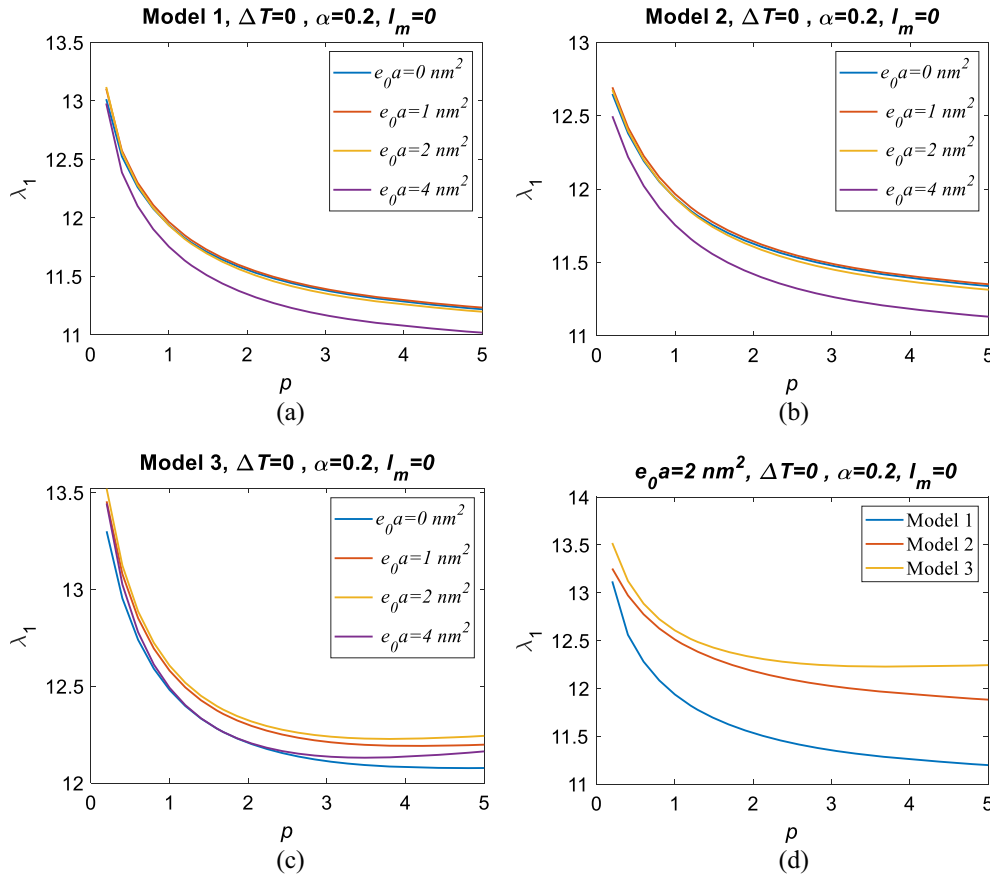
Fig. 24 Variation of the dimensionless frequency λ_1 of material grading index p depending on temperature difference $\Delta T = 0$, porosity $\alpha = 0.2$, the material size factor $l_m = 0$, and different nonlocal $e_0a = 0, 1, 24$

5 Conclusion

This research examined the FG porous beam's behavior exposed to magnetic fields and thermal in terms of free vibration and thermal buckling. The material composition of the investigated FG nanobeam is composed of $BaTiO_3$ at the bottom and $CoFe_2O_4$ at the top. In addition to the magnetic field and thermal effect, the effects of parameters such as the porosity ratio of the nanobeam, material grading index, nonlocal parameter, and material size factor were examined in detail. The effect of material composition, porosity, and nonlinear temperature rise on the effective material properties of the FG nanobeam (thermal expansion, conductivity, and modulus of elasticity) was also investigated.

The motion equations for the nanobeam's free vibration response are obtained using trigonometric higher-order shear deformation theory and taking into account the micromechanical effects of nonlocal differential elasticity and strain grading elasticity. The effects of magnetic field strength, nonlinear temperature, nonlocal parameters, porosity volume fraction, and porosity distribution on the nanobeam's free vibration behavior have been modeled and fully investigated. For porosity distribution functions, symmetric, uniform, and asymmetric ascending downward porosity models are considered. Finally, a summary of the analyses' findings is provided below.

- Effective mechanical parameters alter with nonlinear temperature rise, with thermal expansion coefficient increasing and elastic modulus and thermal conductivity decreasing. The thermal expansion coefficient rises as the material grading index p grows, but the elasticity modulus and thermal conductivity drop. At higher temperatures, the coefficient of thermal conductivity rises; however, it decreases till 750 K. As the porosity ratio α rises, all mechanical qualities drop.

- The material grading index p determines the nanobeam's free vibration response. The nanobeam's magnetostrictive and electro-elastic characteristics depend on $BaTiO_3$ and $CoFe_2O_4$. These components may provide a specialized nanobeam for nanosensors, mechanical sensing devices for nanorobotic grippers, etc.
- As the material grading index p increases, the ratio of $BaTiO_3$ in nanobeams increases, resulting in a decrease in dimensionless frequency. Model 3 frequency drops until material grading index is $p = 2$ and climbs thereafter.
- The porosity ratio greatly impacts the free vibration of FG nanobeams. The porosity ratio rises at all dimensionless frequencies. High volume fractions of $BaTiO_3$ with high porosity ratios will increase dimensionless frequencies in Model 1. As porosity increases, frequencies fall if $p > 1$.
- The aspect ratio of the nanobeam is also crucial. As aspect ratio grows, dimensionless frequencies rise significantly. However, temperature difference strongly affects aspect ratio growth. In a high aspect ratio, $L/h = 50$, dimensionless frequencies diminish and buckling as the temperature difference grows.
- Magnetic and electric potentials alter nanobeam free vibrations. For instance, the all magnetic potential raises dimensionless frequency, whereas the electric potential decreases frequencies. Additionally, when subjected to a magnetic potential, frequencies increase marginally with porosity, whereas when exposed to an electric potential, frequencies increase.
- As the nonlocality effect rises, dimensionless frequencies drop, but frequency increases with material size factor.

Declarations

Conflict of interest The authors declare that they have no conflict of interest.

Appendix A

The eigenvalue equations for trigonometric solution considering general boundary conditions presented in Table 2.

$$\begin{aligned}
&\left[A_{11}\left(r_3 + l_m^2 r_{10}\right) + I_0\omega_n^2\left(r_1 + (e_0a)^2(r_3)\right)\right]U_{mn} - \left[B_{11}\left(r_3 + l_m^2 r_{10}\right) + I_1\omega_n^2 r_1 + (e_0a)^2 I_1\omega_n^2(r_3)\right]W_{bmn} \\
&+\left[-B_{11}^s\left(r_3 + l_m^2 r_{10}\right) + J_1\omega_n^2\left(r_1 + (e_0a)^2(r_3)\right)W_{smn} + A_{31}^e\left(r_1 + l_m^2 r_3\right)\phi_{mn} + A_{31}^m\left(r_1 + l_m^2 r_3\right)Y_{mn} = 0
\end{aligned} \quad (A.1)$$

$$\begin{aligned}
&\left[B_{11}\left(r_9 + l_m^2 r_{11}\right) + I_1\omega_n^2\left(r_7 + (e_0a)^2 r_9\right)\right]U_{mn} \\
&\quad + \left[-D_{11}\left(r_9 + l_m^2 r_{11}\right) - I_2\omega_n^2\left(r_7 + (e_0a)^2 r_9\right)\right. \\
&\qquad +I_0\omega_n^2\left(r_5 + (e_0a)^2 r_7\right) + \left(N^E + N^H + N^T\right)\left(r_7 + (e_0a)^2 r_9\right)\Big]W_{bmn} \\
&\qquad + \Big[-D_{11}^s\left(r_9 + l_m^2 r_{11}\right) \\
&\qquad -I_0\omega_n^2\left(r_5 + (e_0a)^2 r_7\right) + J_2\omega_n^2\left(r_7 + (e_0a)^2 r_9\right) + \left(N^E + N^H + N^T\right)\left(r_7 + (e_0a)^2 r_9\right)\Big]W_{smn} \\
&\qquad + \left[\left(E_{31}^e - A_{15}^e\right)\left(r_7 + l_m^2 r_9\right)\right]\phi_{mn} + \left[\left(E_{31}^m - A_{15}^m\right)\left(r_7 + l_m^2 r_9\right)\right]Y_{mn} = 0
\end{aligned} \quad (A.2)$$

$$\begin{aligned}
&\left[B_{11}^s\left(r_9 + l_m^2 r_{11}\right) + J_1\omega_n^2\left(r_7 + (e_0a)^2 r_9\right)\right]U_{mn} + \Big[-D_{11}^s\left(r_9 + l_m^2 r_{11}\right) - J_2\omega_n^2\left(r_7 + (e_0a)^2 r_9\right) - I_0\omega_n^2\left(r_5 + (e_0a)^2 r_7\right)+) \\
&\quad -D_{11}^s\left(r_9 + l_m^2 r_{11}\right) - I_0\omega_n^2\left(r_5 + (e_0a)^2 r_7\right) + (N^E + N^H + N^T)\left(r_7 + (e_0a)^2 r_9\right)\Big]W_{bmn} \\
&+\Big[A_{44}^s\left(r_7 + l_m^2 r_9\right) - H_{11}^s\left(r_9 + l_m^2 r_{11}\right) + (N^E + N^H + N^T)\left(r_7 + (e_0a)^2 r_9\right)\Big) \\
&\quad -I_0\omega_n^2\left(r_5 + (e_0a)^2 r_7\right) - K_2\omega_n^2\left(\left(r_7 + (e_0a)^2 r_9\right)\right)\Big]W_{smn} \\
&+\left[\left(F_{31}^e - A_{15}^e\right)\left(r_7 + l_m^2 r_9\right)\right]\phi_{mn} + \left(F_{31}^m - A_{15}^m\right)\left(r_7 + l_m^2 r_9\right)Y_{mn} = 0
\end{aligned} \quad (A.3)$$

$$\begin{aligned}
&A_{31}^e\left(r_1 + l_m^2 r_3\right)U_{mn} + \left[-E_{31}^e\left(r_1 + l_m^2 r_3\right)\right]W_{bmn} + \left[\left(F_{31}^e - A_{15}^e\right)\left(r_7 + l_m^2 r_9\right)\right]W_{smn} \\
&\quad +\left[F_{11}^e\left(r_7 + l_m^2 r_9\right) - F_{33}^e\left(r_5 + l_m^2 r_7\right)\right]\phi_{mn} + \left[F_{11}^m\left(r_7 + l_m^2 r_9\right) - F_{33}^m\left(r_5 + l_m^2 r_7\right)\right]Y_{mn} = 0 \\
&A_{31}^m\left(r_1 + l_m^2 r_3\right)U_{mn} - E_{31}^m\left(r_1 + l_m^2 r_3\right)W_{bmn} + \left(E_{15}^m - F_{31}^m\right)\left(r_7 + l_m^2 r_9\right)W_{smn}
\end{aligned} \quad (A.4)$$

$$+ \left[F_{11}^m \left(r_7 + l_m^2 r_9 \right) - F_{33}^m \left(r_5 + l_m^2 r_7 \right) \right] \psi_{mn} + \left[X_{11}^m \left(r_7 + l_m^2 r_9 \right) - X_{33}^m \left(r_5 + l_m^2 r_7 \right) \right] \gamma_{mn} = 0 \qquad (A.5)$$

with

$$r_1 = \int_0^L X_m\prime X_m\prime dx, r_3 = \int_0^L X_m''' X_m\prime dx, r_5 = \int_0^L X_m X_m dx, r_7 = \int_0^L X_m'' X_m dx,$$

$$r_9 = \int_0^L X_m'''' X_m dx, r_{10} = \int_0^L X_m''''' X_m\prime dx, r_{11} = \int_0^L X_m'''''' X_m dx \qquad (A.6)$$

References

1. Ebrahimi, F., Rastgo, A.: An analytical study on the free vibration of smart circular thin FGM plate based on classical plate theory. Thin-Walled Struct. **46**, 1402–1408 (2008). https://doi.org/10.1016/j.tws.2008.03.008
2. Esen, I., Özmen, R.: Free and forced thermomechanical vibration and buckling responses of functionally graded magneto-electro-elastic porous nanoplates. Mech. Based Des. Struct. Mach. (2022). https://doi.org/10.1080/15397734.2022.2152045
3. Eringen, A.C., Edelen, D.G.B.: On nonlocal elasticity. Int. J. Eng. Sci. **10**, 233–248 (1972). https://doi.org/10.1016/0020-7225(72)90039-0
4. Yang, F., Chong, A.C.M., Lam, D.C.C., Tong, P.: Couple stress based strain gradient theory for elasticity. Int. J. Solids Struct. **39**, 2731–2743 (2002). https://doi.org/10.1016/S0020-7683(02)00152-X
5. Akgöz, B., Civalek, Ö.: Longitudinal vibration analysis for microbars based on strain gradient elasticity theory. J. Vib. Control **20**, 606–616 (2014). https://doi.org/10.1177/1077546312463752
6. Kong, S., Zhou, S., Nie, Z., Wang, K.: The size-dependent natural frequency of Bernoulli-Euler micro-beams. Int. J. Eng. Sci. **46**, 427–437 (2008). https://doi.org/10.1016/j.ijengsci.2007.10.002
7. Lim, C.W., Zhang, G., Reddy, J.N.: A higher-order nonlocal elasticity and strain gradient theory and its applications in wave propagation. J. Mech. Phys. Solids **78**, 298–313 (2015). https://doi.org/10.1016/j.jmps.2015.02.001
8. Apuzzo, A., Barretta, R., Faghidian, S.A., Luciano, R., Marotti de Sciarra, F.: Nonlocal strain gradient exact solutions for functionally graded inflected nano-beams. Compos. B Eng. 164, 667–674 (2019). https://doi.org/10.1016/j.compositesb.2018.12.112
9. Esen, I., Abdelrhmaan, A.A., Eltaher, M.A.: Free vibration and buckling stability of FG nanobeams exposed to magnetic and thermal fields. Eng. Comput. (2021). https://doi.org/10.1007/s00366-021-01389-5
10. Esen, I.: Response of a micro-capillary system exposed to a moving mass in magnetic field using nonlocal strain gradient theory. Int. J. Mech. Sci. **188**, 105937 (2020). https://doi.org/10.1016/j.ijmecsci.2020.105937
11. Sladek, J., Sladek, V., Hrcek, S., Pan, E.: The nonlocal and gradient theories for a large deformation of piezoelectric nanoplates. Compos. Struct. **172**, 119–129 (2017). https://doi.org/10.1016/j.compstruct.2017.03.080
12. Abdelrahman, A.A., Esen, I., Daikh, A.A., Eltaher, M.A.: Dynamic analysis of FG nanobeam reinforced by carbon nanotubes and resting on elastic foundation under moving load. Mech. Based Des. Struct. Mach. (2021). https://doi.org/10.1080/15397734.2021.1999263
13. Eringen, A.C.: On differential equations of nonlocal elasticity and solutions of screw dislocation and surface waves. J. Appl. Phys. **54**, 4703–4710 (1983). https://doi.org/10.1063/1.332803
14. Ebrahimi, F., Barati, M.R.: Buckling analysis of smart size-dependent higher order magneto-electro-thermo-elastic functionally graded nanosize beams. J. Mech. **33**, 23–33 (2017). https://doi.org/10.1017/jmech.2016.46
15. Zhong, R., Qin, B., Wang, Q., Shao, W., Shuai, C.: Investigation on flutter instability of magnetic-electric-thermo-elastic functionally graded plates in the supersonic airflow with any yawed angle. Int. J. Mech. Sci. (2021). https://doi.org/10.1016/j.ijmecsci.2021.106356
16. Akgöz, B., Civalek, Ö.: Thermo-mechanical buckling behavior of functionally graded microbeams embedded in elastic medium. Int. J. Eng. Sci. **85**, 90–104 (2014). https://doi.org/10.1016/j.ijengsci.2014.08.011
17. Akgöz, B., Civalek, Ö.: A novel microstructure-dependent shear deformable beam model. Int. J. Mech. Sci. **99**, 10–20 (2015). https://doi.org/10.1016/j.ijmecsci.2015.05.003
18. Akgöz, B., Civalek, Ö.: A size-dependent beam model for stability of axially loaded carbon nanotubes surrounded by Pasternak elastic foundation. Compos. Struct. **176**, 1028–1038 (2017). https://doi.org/10.1016/j.compstruct.2017.06.039
19. Roque, C.M.C., Ferreira, A.J.M., Reddy, J.N.: Analysis of Timoshenko nanobeams with a nonlocal formulation and meshless method. Int. J. Eng. Sci. **49**, 976–984 (2011). https://doi.org/10.1016/j.ijengsci.2011.05.010
20. Xu, X.J., Wang, X.C., Zheng, M.L., Ma, Z.: Bending and buckling of nonlocal strain gradient elastic beams. Compos. Struct. **160**, 366–377 (2017). https://doi.org/10.1016/j.compstruct.2016.10.038
21. Li, L., Hu, Y.: Buckling analysis of size-dependent nonlinear beams based on a nonlocal strain gradient theory. Int. J. Eng. Sci. **97**, 84–94 (2015). https://doi.org/10.1016/j.ijengsci.2015.08.013
22. Nematollahi, M.S., Mohammadi, H., Nematollahi, M.A.: Thermal vibration analysis of nanoplates based on the higher-order nonlocal strain gradient theory by an analytical approach. Superlattices Microstruct. **111**, 944–959 (2017). https://doi.org/10.1016/j.spmi.2017.07.055
23. Karami, B., Janghorban, M., Rabczuk, T.: Static analysis of functionally graded anisotropic nanoplates using nonlocal strain gradient theory. Compos. Struct. **227**, 111249 (2019). https://doi.org/10.1016/j.compstruct.2019.111249
24. Žur, K.K., Arefi, M., Kim, J., Reddy, J.N.: Free vibration and buckling analyses of magneto-electro-elastic FGM nanoplates based on nonlocal modified higher-order sinusoidal shear deformation theory. Compos. B Eng. (2020). https://doi.org/10.1016/j.compositesb.2019.107601

25. Pradhan, S.C., Phadikar, J.K.: Nonlocal elasticity theory for vibration of nanoplates. J. Sound Vib. **325**, 206–223 (2009). https://doi.org/10.1016/j.jsv.2009.03.007

26. Monaco, G.T., Fantuzzi, N., Fabbrocino, F., Luciano, R.: Trigonometric solution for the bending analysis of magneto-electro-elastic strain gradient nonlocal nanoplates in hygro-thermal environment. Mathematics (2021). https://doi.org/10.3390/math9050567

27. Farajpour, A., Hairi Yazdi, M.R., Rastgoo, A., Loghmani, M., Mohammadi, M.: Nonlocal nonlinear plate model for large amplitude vibration of magneto-electro-elastic nanoplates. Compos. Struct. **140**, 323–336 (2016). https://doi.org/10.1016/j.compstruct.2015.12.039

28. Arefi, M., Zenkour, A.M.: Size-dependent free vibration and dynamic analyses of piezo-electro-magnetic sandwich nanoplates resting on viscoelastic foundation. Phys. B Condens. Matter. **521**, 188–197 (2017). https://doi.org/10.1016/j.physb.2017.06.066

29. Li, L., Li, X., Hu, Y.: Free vibration analysis of nonlocal strain gradient beams made of functionally graded material. Int. J. Eng. Sci. **102**, 77–92 (2016). https://doi.org/10.1016/j.ijengsci.2016.02.010

30. Chen, Y., Ye, T., Jin, G., Li, S., Yang, C.: Vibration analysis of rotating pretwist FG sandwich blades operating in thermal environment. Int. J. Mech. Sci. **205**, 106596 (2021). https://doi.org/10.1016/j.ijmecsci.2021.106596

31. Bagheri, E., Asghari, M., Kargarzadeh, A., Badiee, M.: Small-scale oriented elasticity modeling of functionally graded rotating micro-disks with varying angular velocity in the context of the strain gradient theory. Acta Mech. **232**, 2395–2416 (2021). https://doi.org/10.1007/s00707-021-02945-2

32. Albas, ŞD., Ersoy, H., Akgöz, B., Civalek, Ö.: Dynamic analysis of a fiber-reinforced composite beam under a moving load by the ritz method. Mathematics (2021). https://doi.org/10.3390/math9091048

33. Civalek, Ö., Uzun, B., Yaylı, M.Ö.: An effective analytical method for buckling solutions of a restrained FGM nonlocal beam. Comput. Appl. Math. **41**, 1–20 (2022). https://doi.org/10.1007/s40314-022-01761-1

34. Xu, Y., Wei, P., Zhao, L.: Flexural waves in nonlocal strain gradient high-order shear beam mounted on fractional-order viscoelastic Pasternak foundation. Acta Mech. **233**, 4101–4118 (2022). https://doi.org/10.1007/s00707-022-03334-z

35. Li, G.E., Kuo, H.Y.: Effects of strain gradient and electromagnetic field gradient on potential and field distributions of multiferroic fibrous composites. Acta. Mech. **232**, 1353–1378 (2021). https://doi.org/10.1007/s00707-020-02910-5

36. Abouelregal, A.E., Akgöz, B., Civalek, O.: Magneto-thermoelastic interactions in an unbounded orthotropic viscoelastic solid under the Hall current effect by the fourth-order Moore-Gibson-Thompson equation. Comput. Math. Appl. **141**, 102–115 (2023). https://doi.org/10.1016/j.camwa.2023.04.001

37. Akgöz, B., Civalek, Ö.: Bending analysis of embedded carbon nanotubes resting on an elastic foundation using strain gradient theory. Acta Astronaut. **119**, 1–12 (2016). https://doi.org/10.1016/j.actaastro.2015.10.021

38. Demir, Ç., Mercan, K., Numanoglu, H.M., Civalek, Ö.: Bending response of nanobeams resting on elastic foundation. J. Appl. Comput. Mech. **4**, 105–114 (2018). https://doi.org/10.22055/jacm.2017.22594.1137

39. Liu, G., Wu, S., Shahsavari, D., Karami, B., Tounsi, A.: Dynamics of imperfect inhomogeneous nanoplate with exponentially-varying properties resting on viscoelastic foundation. Eur. J. Mech. A/Solids. **95**, 104649 (2022). https://doi.org/10.1016/j.euromechsol.2022.104649

40. Cuong-Le, T., Nguyen, K.D., Le-Minh, H., Phan-Vu, P., Nguyen-Trong, P., Tounsi, A.: Nonlinear bending analysis of porous sigmoid FGM nanoplate via IGA and nonlocal strain gradient theory. Adv. Nano Res. **12**, 441–455 (2022). https://doi.org/10.12989/anr.2022.12.5.441

41. Kumar, Y., Gupta, A., Tounsi, A.: Size-dependent vibration response of porous graded nanostructure with FEM and nonlocal continuum model. Adv. Nano Res. **11**, 1–17 (2021). https://doi.org/10.12989/anr.2021.11.1.001

42. Addou, F.Y., Bourada, F., Meradjah, M., Bousahla, A.A., Tounsi, A., Ghazwani, M.H., Alnujaie, A.: Impact of porosity distribution on static behavior of functionally graded plates using a simple quasi-3D HSDT. Comput. Concr. **32**, 87–97 (2023)

43. Alsubaie, A.M., Alfaqih, I., Al-Osta, M.A., Tounsi, A., Chikh, A., Mudhaffar, I.M., Tahir, S.: Porosity-dependent vibration investigation of functionally graded carbon nanotube-reinforced composite beam. Comput. Concr. **32**, 75–85 (2023)

44. Bourada, F., Bousahla, A.A., Tounsi, A., Tounsi, A., Tahir, S.I., Al-Osta, M.A., Do-Van, T.: An integral quasi-3D computational model for the hygro-thermal wave propagation of imperfect FGM sandwich plates. Comput. Concr. **32**, 61–74 (2023)

45. Khorasani, M., Lampani, L., Tounsi, A.: A refined vibrational analysis of the FGM porous type beams resting on the silica aerogel substrate. Steel Compos. Struct. **47**, 633–644 (2023). https://doi.org/10.12989/scs.2023.47.5.633

46. Mesbah, A., Belabed, Z., Amara, K., Tounsi, A., Bousahla, A.A., Bourada, F.: Formulation and evaluation a finite element model for free vibration and buckling behaviours of functionally graded porous (FGP) beams. Struct. Eng. Mech. **86**, 291–309 (2023). https://doi.org/10.12989/sem.2023.86.3.291

47. Xia, L., Wang, R.W., Chen, G.C., Asemi, K., Tounsi, A.: The finite element method for dynamics of FG porous truncated conical panels reinforced with graphene platelets based on the 3 3-D elasticity. Adv. Nano Res. **14**, 375–389 (2023). https://doi.org/10.12989/anr.2023.14.4.375

48. Hadji, M., Bouhadra, A., Mamen, B., Menasria, A.: Combined influence of porosity and elastic foundation parameters on the bending behavior of advanced sandwich structures. Steel Compos. Struct. **46**, 1–13 (2023)

49. Katiyar, V., Gupta, A., Tounsi, A.: Microstructural/geometric imperfection sensitivity on the vibration response of geometrically discontinuous bi-directional functionally graded plates (2D-FGPs) with partial supports by using FEM. Steel Compos. Struct. **35**, 621–640 (2022). https://doi.org/10.12989/scs.2022.45.5.621

50. Van Vinh, P., Van Chinh, N., Tounsi, A.: Static bending and buckling analysis of bi-directional functionally graded porous plates using an improved first-order shear deformation theory and FEM. Eur. J. Mech. A/Solids. **96**, 104743 (2022). https://doi.org/10.1016/j.euromechsol.2022.104743

51. Arshid, E., Khorasani, M., Soleimani-Javid, Z., Amir, S., Tounsi, A.: Porosity-dependent vibration analysis of FG microplates embedded by polymeric nanocomposite patches considering hygrothermal effect via an innovative plate theory. Eng. Comput. **38**, 4051–4072 (2022). https://doi.org/10.1007/s00366-021-01382-y

52. Al-Osta, M.A., Saidi, H., Tounsi, A., Al-Dulaijan, S.U., Al-Zahrani, M.M., Sharif, A., Tounsi, A.: Influence of porosity on the hygro-thermo-mechanical bending response of an AFG ceramic-metal plates using an integral plate model. Smart Struct. Syst. **28**, 499–513 (2021). https://doi.org/10.12989/sss.2021.28.4.499

53. Bellifa, H., Selim, M.M., Chikh, A., Bousahla, A.A., Bourada, F., Tounsi, A., Benrahou, K.H., Al-Zahrani, M.M., Tounsi, A.: Influence of porosity on thermal buckling behavior of functionally graded beams. Smart Struct. Syst. **27**, 719–728 (2021). https://doi.org/10.12989/sss.2021.27.4.719

54. Bekkaye, T.H.L., Fahsi, B., Bousahla, A.A., Bourada, F., Tounsi, A., Benrahou, K.H., Tounsi, A., Al-Zahrani, M.M.: Porosity-dependent mechanical behaviors of FG plate using refined trigonometric shear deformation theory. Comput. Concr. **26**, 439–450 (2020). https://doi.org/10.12989/cac.2020.26.5.439

55. Cheshmeh, E., Karbon, M., Eyvazian, A., Jung, D. won, Habibi, M., Safarpour, M.: Buckling and vibration analysis of FG-CNTRC plate subjected to thermo-mechanical load based on higher order shear deformation theory. Mech. Based Des. Struct. Mach. **50**, 1137–1160 (2022). https://doi.org/10.1080/15397734.2020.1744005

56. Esen, I., Özmen, R.: Thermal vibration and buckling of magneto-electro-elastic functionally graded porous nanoplates using nonlocal strain gradient elasticity. Compos. Struct. (2022). https://doi.org/10.1016/j.compstruct.2022.115878

57. Vaezi, M., Shirbani, M.M., Hajnayeb, A.: Free vibration analysis of magneto-electro-elastic microbeams subjected to magneto-electric loads. Phys. E Low-Dimension. Syst. Nanostruct. **75**, 280–286 (2016). https://doi.org/10.1016/j.physe.2015.09.019

58. Toro, R.D., Bacigalupo, A., Lepidi, M., Mazzino, A.: Dispersive waves in magneto-electro-elastic periodic waveguides. Int. J. Mech. Sci. **236**, 107759 (2022). https://doi.org/10.1016/j.ijmecsci.2022.107759

59. Dat, N.D., Quan, T.Q., Mahesh, V., Duc, N.D.: Analytical solutions for nonlinear magneto-electro-elastic vibration of smart sandwich plate with carbon nanotube reinforced nanocomposite core in hygrothermal environment. Int. J. Mech. Sci. **186**, 105906 (2020). https://doi.org/10.1016/j.ijmecsci.2020.105906

60. Ke, L.L., Wang, Y.S., Wang, Z.D.: Thermal effect on free vibration and buckling of size-dependent microbeams. Phys. E Low-Dimension. Syst. Nanostruct. **43**, 1387–1393 (2011). https://doi.org/10.1016/j.physe.2011.03.009

61. Eltaher, M.A., Emam, S.A., Mahmoud, F.F.: Free vibration analysis of functionally graded size-dependent nanobeams. Appl. Math. Comput. **218**, 7406–7420 (2012). https://doi.org/10.1016/j.amc.2011.12.090

62. Monaco, G.T., Fantuzzi, N., Fabbrocino, F., Luciano, R.: Critical temperatures for vibrations and buckling of magneto-electro-elastic nonlocal strain gradient plates. Nanomaterials **11**, 1–18 (2021). https://doi.org/10.3390/nano11010087

63. Chen, B., Xu, Q., Zhu, B., Yang, Y., Li, Y.: Buckling and postbuckling behaviors of symmetric/asymmetric double-beam systems. Int. J. Mech. Sci. (2022). https://doi.org/10.1016/j.ijmecsci.2022.107712

64. Daghigh, H., Daghigh, V., Milani, A., Tannant, D., Lacy, T.E., Reddy, J.N.: Nonlocal bending and buckling of agglomerated CNT-Reinforced composite nanoplates. Compos. B Eng. **183**, 107716 (2020). https://doi.org/10.1016/j.compositesb.2019.107716

65. Boyina, K., Piska, R., Natarajan, S.: Nonlocal strain gradient model for thermal buckling analysis of functionally graded nanobeams. Acta Mech. (2023). https://doi.org/10.1007/s00707-023-03637-9

66. Quan, T.Q., Dat, N.D., Duc, N.D.: Static buckling, vibration analysis and optimization of nanocomposite multilayer perovskite solar cell. Acta Mech. **234**, 3893–3915 (2023). https://doi.org/10.1007/s00707-023-03588-1

67. Kiran, M.C., Kattimani, S.C.: Assessment of porosity influence on vibration and static behaviour of functionally graded magneto-electro-elastic plate: A finite element study. Eur. J. Mech. A/Solids. **71**, 258–277 (2018). https://doi.org/10.1016/j.euromechsol.2018.04.006

68. Liu, J., Zhang, P., Lin, G., Wang, W., Lu, S.: High order solutions for the magneto-electro-elastic plate with non-uniform materials. Int. J. Mech. Sci. **115–116**, 532–551 (2016). https://doi.org/10.1016/j.ijmecsci.2016.07.033

69. Ebrahimi, F., Jafari, A., Barati, M.R.: Vibration analysis of magneto-electro-elastic heterogeneous porous material plates resting on elastic foundations. Thin-Walled Struct. **119**, 33–46 (2017). https://doi.org/10.1016/j.tws.2017.04.002

70. Xue, Y., Jin, G., Ma, X., Chen, H., Ye, T., Chen, M., Zhang, Y.: Free vibration analysis of porous plates with porosity distributions in the thickness and in-plane directions using isogeometric approach. Int. J. Mech. Sci. **152**, 346–362 (2019). https://doi.org/10.1016/j.ijmecsci.2019.01.004

71. Wang, Y.Q., Zu, J.W.: Vibration behaviors of functionally graded rectangular plates with porosities and moving in thermal environment. Aerosp. Sci. Technol. **69**, 550–562 (2017). https://doi.org/10.1016/j.ast.2017.07.023

72. Li, Z., Xu, Y., Huang, D.: Analytical solution for vibration of functionally graded beams with variable cross-sections resting on Pasternak elastic foundations. Int. J. Mech. Sci. **191**, 106084 (2021). https://doi.org/10.1016/j.ijmecsci.2020.106084

73. Kumar, P., Harsha, S.P.: Vibration response analysis of sigmoidal functionally graded piezoelectric (FGP) porous plate under thermo-electric environment. Mech. Based Des. Struct. Mach. (2021). https://doi.org/10.1080/15397734.2021.1971090

74. Allah Gholi, A.M., Khorshidvand, A.R., Jabbari, M., Khorsandijou, S.M.: Magneto-electro-thermo-elastic frequency response of functionally graded saturated porous annular plates via trigonometric shear deformation theory. Acta Mech. **234**, 3665–3685 (2023). https://doi.org/10.1007/s00707-023-03530-5

75. Sui, Y., Wang, W., Zhang, H.: Effects of electromagnetic fields on the contact of magneto-electro-elastic materials. Int. J. Mech. Sci. **223**, 107283 (2022). https://doi.org/10.1016/j.ijmecsci.2022.107283

76. Esmaeilzadeh, M., Kadkhodayan, M.: Numerical investigation into dynamic behaviors of axially moving functionally graded porous sandwich nanoplates reinforced with graphene platelets. Mater. Res. Express. (2019). https://doi.org/10.1088/2053-1591/ab407b

77. Bui, X., Nguyen, T., Nguyen, P.T.T.: Stochastic vibration and buckling analysis of functionally graded sandwich thin-walled beams. Mech. Based Des. Struct. Mach. (2023). https://doi.org/10.1080/15397734.2023.2165101

78. Xu, X., Karami, B., Shahsavari, D.: Time-dependent behavior of porous curved nanobeam. Int. J. Eng. Sci. (2021). https://doi.org/10.1016/j.ijengsci.2021.103455

79. Ebrahimi, F., Hosseini, S.H.S.: Resonance analysis on nonlinear vibration of piezoelectric/FG porous nanocomposite subjected to moving load. Eur. Phys. J. Plus. **135**, 1–23 (2020). https://doi.org/10.1140/epjp/s13360-019-00011-4

80. Li, Z., Wang, Q., Qin, B., Zhong, R., Yu, H.: Vibration and acoustic radiation of magneto-electro-thermo-elastic functionally graded porous plates in the multi-physics fields. Int. J. Mech. Sci. (2020). https://doi.org/10.1016/j.ijmecsci.2020.105850

81. Li, Z., Zhong, R., Wang, Q., Qin, B., Yu, H.: The thermal vibration characteristics of the functionally graded porous stepped cylindrical shell by using characteristic orthogonal polynomials. Int. J. Mech. Sci. **182**, 105779 (2020). https://doi.org/10.1016/j.ijmecsci.2020.105779

82. Chen, D., Yang, J., Kitipornchai, S.: Free and forced vibrations of shear deformable functionally graded porous beams. Int. J. Mech. Sci. **108–109**, 14–22 (2016). https://doi.org/10.1016/j.ijmecsci.2016.01.025

83. Majdi, A., Yasin, Y., Altalbawy, F.M.A., Mashhadani, Z.I. Al, Albahash, Z.F., Ahmadi, S., Majdi, A., Yasin, Y., Altalbawy, F.M.A.: Size-dependent vibrations of bi-directional functionally graded porous beams under moving loads incorporating thickness effect. Mech. Based Des. Struct. Mach. (2023). https://doi.org/10.1080/15397734.2023.2165098

84. Karami, B., Janghorban, M., Rabczuk, T.: Dynamics of two-dimensional functionally graded tapered Timoshenko nanobeam in thermal environment using nonlocal strain gradient theory. Compos. Part B Eng. **182**, 107622 (2020). https://doi.org/10.1016/j.compositesb.2019.107622

85. Lu, L., Guo, X., Zhao, J.: Size-dependent vibration analysis of nanobeams based on the nonlocal strain gradient theory. Int. J. Eng. Sci. **116**, 12–24 (2017). https://doi.org/10.1016/j.ijengsci.2017.03.006

86. Yang, W., Wang, S., Kang, W., Yu, T., Li, Y.: A unified high-order model for size-dependent vibration of nanobeam based on nonlocal strain/stress gradient elasticity with surface effect. Int. J. Eng. Sci. **182**, 103785 (2023). https://doi.org/10.1016/j.ijengsci.2022.103785

87. Van Vinh, P., Tounsi, A.: Free vibration analysis of functionally graded doubly curved nanoshells using nonlocal first-order shear deformation theory with variable nonlocal parameters. Thin-Walled Struct. **174**, 109084 (2022). https://doi.org/10.1016/j.tws.2022.109084

88. Civalek, Ö., Ersoy, H., Uzun, B., Yaylı, M.Ö.: Dynamics of a FG porous microbeam with metal foam under deformable boundaries. Acta Mech. (2023). https://doi.org/10.1007/s00707-023-03663-7

89. Khoa, N.D.: Free vibration and nonlinear dynamic behaviors of the imperfect smart electric magnetic FG-laminated composite panel in a hygrothermal environments. Acta Mech. **234**, 2617–2658 (2023). https://doi.org/10.1007/s00707-023-03505-6

90. Mellal, F., Bennai, R., Avcar, M., Nebab, M., Atmane, H.A.: On the vibration and buckling behaviors of porous FG beams resting on variable elastic foundation utilizing higher-order shear deformation theory. Acta Mech. **234**, 3955–3977 (2023). https://doi.org/10.1007/s00707-023-03603-5

91. Karami, B., Janghorban, M.: On the dynamics of porous nanotubes with variable material properties and variable thickness. Int. J. Eng. Sci. **136**, 53–66 (2019). https://doi.org/10.1016/j.ijengsci.2019.01.002

92. Gogotsi, Y.: Nanomaterials Handbook. CRC Press, Second edition. Boca Raton : Taylor & Francis, CRC Press, 2017. Series: Advanced materials and technologies series (2017)

93. Özmen, R., Kılıç, R., Esen, I.: Thermomechanical vibration and buckling response of nonlocal strain gradient porous FG nanobeams subjected to magnetic and thermal fields. Mech. Adv. Mater. Struct. (2022). https://doi.org/10.1080/15376494.2022.2124000

94. Gao, K., Huang, Q., Kitipornchai, S., Yang, J.: Nonlinear dynamic buckling of functionally graded porous beams. Mech. Adv. Mater. Struct. (2021). https://doi.org/10.1080/15376494.2019.1567888

95. Touloukian, Y.S.: Thermophysical properties of high temperature solid materials. Macmillan, New York (1967)

96. Reddy, J.N., Chin, C.D.: Thermomechanical analysis of functionally graded cylinders and plates. J. Therm. Stress. **21**, 593–626 (1998). https://doi.org/10.1080/01495739808956165

97. He, Y.: Heat capacity, thermal conductivity, and thermal expansion of barium titanate-based ceramics. Thermochim. Acta **419**, 135–141 (2004). https://doi.org/10.1016/j.tca.2004.02.008

98. Malikan, M., Wiczenbach, T., Eremeyev, V.A.: Thermal buckling of functionally graded piezomagnetic micro- and nanobeams presenting the flexomagnetic effect. Contin. Mech. Thermodyn. **34**, 1051–1066 (2022). https://doi.org/10.1007/s00161-021-01038-8

99. Touloukian, Y.S., Powell, R.W., Ho, C.Y., P.G.K.: Thermophysical Properties of Matter. In: Thermal Conductivity: Nonmetallic Solids,. IFI/Plenum Press, New York (1970)

100. Dent, A.C., Bowen, C.R., Stevens, R., Cain, M.G., Stewart, M.: Effective elastic properties for unpoled barium titanate. J. Eur. Ceram. Soc. **27**, 3739–3743 (2007). https://doi.org/10.1016/j.jeurceramsoc.2007.02.031

101. Kiani, Y., Eslami, M.R.R.: An exact solution for thermal buckling of annular FGM plates on an elastic medium. Compos. B Eng. **45**, 101–110 (2013). https://doi.org/10.1016/j.compositesb.2012.09.034

102. Zhang, D.G.: Thermal post-buckling and nonlinear vibration analysis of FGM beams based on physical neutral surface and high order shear deformation theory. Meccanica **49**, 283–293 (2014). https://doi.org/10.1007/s11012-013-9793-9

103. Ebrahimi, F., Barati, M.R.: A nonlocal higher-order refined magneto-electro-viscoelastic beam model for dynamic analysis of smart nanostructures. Int. J. Eng. Sci. **107**, 183–196 (2016). https://doi.org/10.1016/j.ijengsci.2016.08.001

104. Ebrahimi, F., Barati, M.R.: Hygrothermal buckling analysis of magnetically actuated embedded higher order functionally graded nanoscale beams considering the neutral surface position. J. Therm. Stress. **39**, 1210–1229 (2016). https://doi.org/10.1080/01495739.2016.1215726

105. Fleck, N.A., Muller, G.M., Ashby, M.F., Hutchinson, J.W.: Strain gradient plasticity: Theory and experiment. Acta Metall. Mater. **42**, 475–487 (1994). https://doi.org/10.1016/0956-7151(94)90502-9

106. Miandoab, E.M., Yousefi-Koma, A., Pishkenari, H.N.: Nonlocal and strain gradient based model for electrostatically actuated silicon nano-beams. Microsyst. Technol. **21**, 457–464 (2015). https://doi.org/10.1007/s00542-014-2110-2

107. Ebrahimi, F.: Dynamic modeling of a thermo – piezo-electrically actuated nanosize beam subjected to a magnetic field. Appl. Phys. A **122**, 1–18 (2016). https://doi.org/10.1007/s00339-016-0001-3

108. Rahmani, O., Pedram, O.: Analysis and modeling the size effect on vibration of functionally graded nanobeams based on nonlocal Timoshenko beam theory. Int. J. Eng. Sci. **77**, 55–70 (2014). https://doi.org/10.1016/j.ijengsci.2013.12.003

109. Ebrahimi, F., Salari, E.: Thermo-mechanical vibration analysis of nonlocal temperature-dependent FG nanobeams with various boundary conditions. Compos. B Eng. **78**, 272–290 (2015). https://doi.org/10.1016/j.compositesb.2015.03.068

110. Ebrahimi, F., Salari, E.: Thermal buckling and free vibration analysis of size dependent Timoshenko FG nanobeams in thermal environments. Compos. Struct. **128**, 363–380 (2015). https://doi.org/10.1016/j.compstruct.2015.03.023